Tailoring osteoimmunity and hemostasis using 3D-Printed nano-photocatalytic bactericidal scaffold for augmented bone regeneration

Sayan Deb Dutta [a,b,c,1], Jin Hexiu [d,1], Md Moniruzzaman [e,1], Tejal V. Patil [a,f], Rumi Acharya [a,f], Jong Sung Kim [e,**], Ki-Taek Lim [a,b,f,*]

[a] Department of Biosystems Engineering, Kangwon National University, Chuncheon, 24341, Republic of Korea
[b] Institute of Forest Science, Kangwon National University, Chuncheon, 24341, Republic of Korea
[c] Center for Surgical Bioengineering, Department of Surgery, School of Medicine, University of California Davis, Sacramento, CA, 95817, United States
[d] Department of Oral and Maxillofacial Surgery, Capital Medical University, Beijing-1000054, China
[e] Department of Chemical and Biological Engineering, Gachon University, Seongnam, 13120, Republic of Korea
[f] Interdisciplinary Program in Smart Agriculture, Kangwon National University, Chuncheon, 24341, Republic of Korea

ARTICLE INFO

ABSTRACT

Bone hemorrhage, infection, and large bone defects following surgical treatment of traumatic bone injury have raised potential concerns, underscoring the urgent need to develop multifunctional therapeutic platforms that can effectively address traumatic bone regeneration. Advancements in three-dimensional (3D) printing technology have propelled the development of several engineering disciplines, such as tissue engineering. Nevertheless, 3D-printed frameworks with conventional materials often lack multifunctional capabilities to promote specific activities for diverse regeneration purposes. In this study, we developed a highly oxidized two-dimensional (2D) graphitic carbon nitride (Ox-gCN) as a nano-photocatalyst to reinforce alginate/gelatin (ALG)-based hydrogel scaffolds (ALG/CN) to achieve an anti-inflammatory and osteo-immunomodulatory niche with superior hemostatic ability for traumatic bone injury repair. Sulfuric acid oxidation enhances the oxygen-containing functional groups of the g-CN surface and promotes cell adhesion and differentiation of human bone marrow-derived mesenchymal stem cells (hBMSCs) *in vitro*. Moreover, the excellent visible light-activated photocatalytic characteristics of the ALG/CN scaffold were used in antibacterial studies. In addition, the ALG/CN bio/nanocomposite scaffold facilitates M2 polarization of macrophages than did pristine ALG scaffolds. Furthermore, ALG/CN scaffold induced hBMSCs differentiation by upregulating ERK and MAPKs phosphorylation during osteo-immunomodulation. In a rat calvaria defect model, the fabricated ALG/CN scaffolds induced new bone formation through collagen deposition and activation of osteocalcin proteins without inflammation *in vivo*. These results highlight the potential of 3D-printed functionalized 2D carbon nitrides in regulating the bone immune microenvironment, which may be beneficial for developing advanced tissue constructs, especially for traumatic bone regeneration in clinical settings.

1. Introduction

Regeneration of traumatic bone injury and hemorrhage in clinical settings remains challenging because of the limited availability of patient-specific orthopedic implants that can help regenerate large bone defects with a continuous supply of nutrients and oxygen to stem cells in the defect region [1]. Current regenerative strategies include the use of several autografts, allografts, and various polymeric scaffolds, which can induce bone regeneration to a certain extent; however, they often lack multi-faceted functionalities, such as hemostasis function, post-surgical infection prevention, angiogenic capability, and immuno-modulatory performances [2]. In recent years, three-dimensional (3D) printing technology has revolutionized biomedical engineering, especially its ability to design patient-specific grafts through rapid proto-typing [3]. The 3D-printed scaffolds, designed with diverse surface topographies, functional groups, porosity, and wettability, facilitate the

---

infiltration and proliferation/differentiation of the bone and immune cells, thereby accelerating bone regeneration [2b,4]. Increased scaffold porosity increases the surface area for bone cell adherence and promotes a faster degradation rate due to reduced mass/volume, thereby playing a crucial role in tissue regeneration [5]. To date, most orthopedic implants used for 3D printing are fabricated using typical polymeric compounds, such as bioceramics (*e.g.*, pristine and metal-doped hydroxyapatites) [1a,6], bioactive glasses [1c,7] [7], titania-based ceramics [8], and various biodegradable biopolymers [9], However, these materials lack robust functionality to facilitate optimal bone regeneration due to less affinity to the stem cells, slow biodegradability (*e.g.*, when more than two/three biopolymers are used), less immunomodulatory activities (*e. g.*, poor adhesion of macrophages or platelets), and a slow rate of osteogenesis. Therefore, 3D-printed orthopedic implants require further modification to facilitate rapid and effective immunomodulatory bone regeneration.

To address these limitations, various types of two-dimensional (2D) and 2D hetero/nanocomposite materials can be incorporated with printable hydrogel inks to improve mechanical, structural, and biological properties [10]. 2D materials consist of a single or a few atomic layers, allowing unrestricted electron flow in the two dimensions that are not within the nanoscale range (<100 nm) [11]. Given their nanoscale size, tunable surface functional groups, exceptional physiochemical and optical properties, light-harvesting abilities, and excellent biocompatibility, 2D materials such as black phosphorus (BP), graphene oxide (GO), titanium carbides (Ti_3C_2-MXenes), boron nitrides (BNs), molybdenum sulfide (MoS_2), and other transition metal dichalcogenides (TMDCs) has been used to reinforce 3D-printed scaffolds for use in tissue engineering applications [11b]. Among the various 2D materials, graphitic carbon nitride (g-CN), a semiconductor nanomaterial, has gained considerable attention in tissue engineering owing to its exceptional physicochemical properties, including tunable surface and optical properties, low density, higher stability, and improved bioactivity [12]. The g-CN is a promising 2D material with a unique electronic structure of carbon-nitrogen (C–N) heterocycles that has diverse applications, such as photocatalysis, energy storage, electromagnetic shielding, water purification, toxic pollutant removal, and reinforcing the mechanical properties of scaffolds [13]. The excellent responsiveness of g-CN to visible light and near-infrared makes it an ideal material for designing and fabricating nanocatalytic scaffolding platforms for antibacterial therapy [12,14] and bioimaging probes [15] for tissue engineering applications. Bulk g-CN and its nanocomposites

facilitate effective bone regeneration [16]. For instance, Liu et al. [17] reported that strontium (Sr^{2+})-doped g-CN nanosheets induce bone regeneration by inducing osteogenic transcription factors and enhancing the binding of focal adhesion kinases (FAKs) of human bone mesenchymal stem cells (hBMSCs). Furthermore, a g-CN/GO nanocomposite was used to investigate the critical-sized bone defect in rabbit femur [18]. The selective oxidation of bulk g-CN may facilitate oxygen-rich domains, resulting in a porous g-CN structure with enhanced surface area, which improves cell adherence, biocompatibility, and tissue regenerative capabilities [19]. A comparative analysis of various 2D and 3D nanomaterial-reinforced printable hydrogels for bone regeneration is summarized in Table S1.

Bulk g-CN has demonstrated excellent visible light-harvesting capabilities for antibacterial applications and accelerating bone regeneration. Recently, Papaioannou et al. reported that g-CN/nHAp-reinforced 3D-printed hydrogels exhibited good biocompatibility and promoted tissue regeneration [20]. However, the potential of g-CN in enhancing 3D printability and immunomodulation-assisted bone regeneration remains unclear. This study explored the multifunctional tissue-regenerative ability of highly oxidized and water-soluble g-CN-reinforced biopolymer hydrogel scaffolds with tunable physicochemical properties for traumatic bone regeneration (Scheme 1). Our previous study highlighted the excellent 3D printability of Alg/Gel double-network hydrogels for *in vivo* bone regeneration [3a]. The novelty of this study was the incorporation of visible-light-active, highly oxidized g-CN (Ox-gCN) to reinforce the alginate/gelatin (Alg/Gel) hydrogels, where Ox-gCN was also serving as a nano-photocatalyst. The resulting hydrogel scaffolds were mechanically robust and highly hydrophilic, providing favorable nano/biointerfaces for the growth and differentiation of hBMSCs. Moreover, the incorporation of Ox-gCN into the Alg/Gel matrix (ALG/CN) induced the proliferation of murine monocytes/macrophages (RAW 264.7 cells) and facilitated anti-inflammatory (M2 polarization) activation, which in turn facilitated osteo-immunomodulation and immediate hemostasis (<2 min) than those of commercial hemostats. In addition, the visible light-responsiveness of the ALG/CN hybrid scaffold was utilized to evaluate its antibacterial performance against gram-negative (*E. coli*) and gram-positive (*S. epidermidis*) bacteria, highlighting its potential as an effective disinfectant. In a calvaria-critical cranial defect model, application of the ALG/CN scaffold enhanced *in vivo* bone regeneration by inducing collagen deposition and osteocalcin secretion, further suggesting its bone regeneration ability. This study demonstrated a
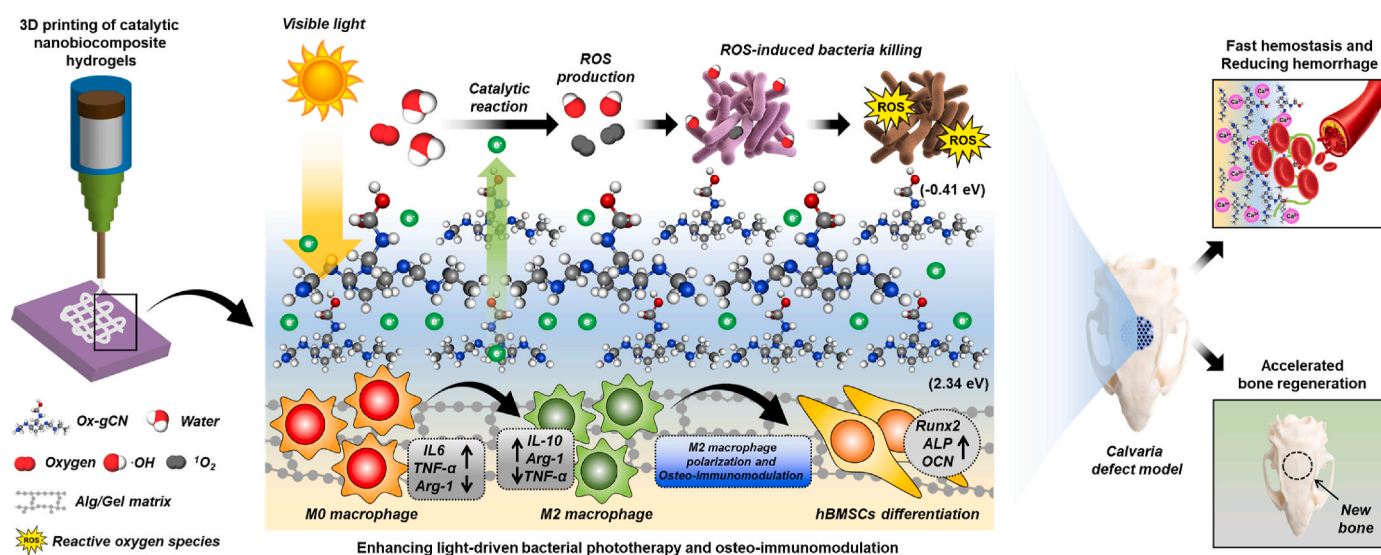
Scheme 1. Schematic illustration of the ultrasmall graphitic carbon nitride-decorated 3D printed oxygen-containing scaffolds for visible light-activated bacterial biofilm eradication, rapid hemostasis, and immunomodulatory bone regeneration.

promising strategy for multifunctional bone regeneration in precision medicine by attenuating blood loss, surgical infections, and osteo-immunomodulation.

2. Results and discussion

2.1. Characterization of g-CN and Ox-gCN

Ultra-small Ox-gCN was synthesized from g-CN using a modified Hummer's method, which is a simple and eco-friendly oxygen-doping method with improved biological properties (Fig. S1(a)). Ox-gCN was used to fabricate a biocompatible hydrogel ink with improved physicochemical properties to reduce hemorrhage, antibiosis, and for applications in bone tissue engineering. Schematic illustration of the Ox-gCN synthesis and the fabrication of the composite hydrogel inks is shown in Fig. 1(a). Sulfuric acid acted as an intercalating and oxidizing agent for g-CN. A 60-min oxidation time for Ox-gCN was selected to achieve a higher oxygen doping on the g-CN surfaces [14a]. The morphologies of the synthesized g-CN and Ox-gCN were investigated through field emission scanning electron microscopy (FE-SEM), high resolution transmission electron microscopy (HR-TEM), and atomic force microscopy (AFM). As shown in Fig. 1(b) and Fig. S2(a), bulk g-CN exhibited unique nanosheet-like structures. However, sulfuric acid oxidation and ultrasonication produced smaller particles with pit-like Ox-gCN structures, which demonstrated a higher degree of oxidation and surface defects with greater dispersion ability than g-CN. Energy-dispersive X-ray spectroscopy (EDS) revealed a difference in oxygen content between g-CN and Ox-gCN. Bulk g-CN has an average oxygen content of 6.14 wt %, whereas Ox-gCN exhibited an average oxygen content of 11.31 wt%, indicating a more homogenous distribution of oxygen onto the surface. Trace amount of sulfur (0.027 wt%) was detected on the Ox-gCN surface due to the sulfuric acid intercalation, which was absent in pure g-CN. Further morphological analysis using HR-TEM and AFM spectroscopy confirmed the intrinsic structure. As shown in Fig. 1(c) and Fig. S2(b), pure g-CN exhibited uniform nanosheet layers with a line spacing of 0.21 nm of the (002) plane. In addition, Ox-gCN exhibited a nanoflake-like morphology, aligning with the SEM results.

Furthermore, the structural differences between g-CN and Ox-gCN were confirmed by AFM (Fig. 1(c) and d)). Pure g-CN exhibited a stacked layer of self-assembled nanosheets with an average layer height and thickness of 380 nm and 0.65 nm, respectively. The increased thickness of the multiple nanosheets was attributed to adsorbed water molecules, creating a "dead layer" or intercalation [21]. In contrast, the Ox-gCN exhibited small particles with an average height of 87 nm and a thickness of 0.25 nm, consistent with the FR-SEM data. Surface charge and stability tests were performed to assess the aqueous stability of the particles. As shown in Fig. S2(c), the zeta potentials of the pure g-CN and Ox-gCN were -49.2 ± 0.21 and -59.77 ± 0.42 mV, respectively. The higher electronegativity of Ox-gCN suggests the presence of abundant oxygen moieties on the surface, which allowed greater hydrogen bond formation and dispersion (Fig. S2(d)) in an aqueous medium than that of pure g-CN [45–50]. The dispersion stability of nanoparticles is crucial for printable ink preparation, and a homogenous particle dispersion enables high-resolution printing with improved mechanical properties.

Fourier transform infrared (FT-IR) and X-ray diffraction (XRD) spectroscopy were used to investigate the functional and structural properties of g-CN and Ox-gCN. As shown in Fig. S3(a), the characteristic triazine unit in g-CN at approximately 814 cm^{-1} was gradually decreased in Ox-gCN due to surface oxidation. Interestingly, the stretching vibration at approximately 889 cm^{-1} in g-CN was assigned to the hydrogen atom bound to the triazine framework, which gradually decreased in the Ox-gCN due to replacement with oxygen-containing functional groups [22]. The Ox-gCN exhibited signature C=N vibrations of nitrogen heterocycles within the 1350–1700 cm^{-1} range, which is much narrower than that of bulk g-CN. Moreover, the stretching vibration at 1043 cm^{-1} attributed to the carbonyl (C=O) groups in

Ox-gCN confirmed the oxidation of g-CN nanosheets. The effect of sulfuric-acid oxidation on the structural alteration of Ox-gCN was confirmed by XRD, and the results are shown in Fig. S3(b). In bulk g-CN, the origin of the diffraction peak at 2θ = 12.8° was due to the inter-planar structural pattern (lamellar structure) for the (001) plane of the graphitic carbon nitride, and a sharp and highly crystalline peak located at 2θ = 27.56° was due to the inter-layer diffraction pattern for the (002) plane of the graphite-like structures [22a,23] [23]. Notably, the diffraction peak at 2θ = 12.8° was gradually shifted to a more broad peak at 2θ = 13.78°, suggesting that sulfuric acid intercalation and oxidation for 60 min results in structural alteration by destroying the C=N bonds and thereby losing the lamellar structure. Furthermore, the characteristic peak at 2θ = 27.56° in g-CN was decreased to 2θ = 27.71° after oxidation, with a wide full width at half maxima (FWHM), suggesting the decrease in crystallinity after oxygen functionalization, which aligns with those observed in oxidized graphitic compounds [24]. These findings corroborate the findings of FE-SEM and HR-TEM.

Next, we analyzed the XPS profiles of the bulk g-CN and Ox-gCN to investigate their elemental states and oxygen-containing functional groups. The XPS survey spectra (Fig. S4(a)) of the bulk g-CN revealed three characteristic peaks at approximately 287.75 eV, 398.67 eV, and 531.02 eV, corresponding to the C1s (37.06 wt%), N1s (54.17 wt%), and O1s (1.66 wt%) spectra, respectively. Interestingly, an additional peak (at approximately 196.65 eV in Ox-gCN appeared for S2p (-SO₃H) indicating sulfuric acid oxidation. Additionally, in Ox-gCN, a gradual increase in the oxygen content (8.29 wt%) was observed with a decrease in carbon (37.06 wt%) and nitrogen (53.43 wt%) contents at C1s and N1s, suggesting successful oxygen functionalization of the g-CN framework, aligning with the XRD data. Moreover, the integrated area ratio of O1s and C1s peak in g-CN and Ox-gCN increased from 0.04 to 0.22, further suggesting oxygen doping into the carbon nitride framework. High-resolution XPS analysis was performed to understand oxygen doping in the g-CN matrix. As shown in Fig. S4(b), the high-resolution N1s spectra of the bulk g-CN were deconvoluted into three main peaks at approximately 397.1 eV, 399.8 eV, and 403.6 eV, corresponding to N^{3-}/-C ≡ N, C=N–C, and N-(C)₃, respectively, indicative of pyridinic-N and ternary-N groups, respectively. Moreover, Ox-gCN exhibited characteristic peaks at approximately 397.2 eV, 397.8 eV, and 399.1 eV, corresponding to the N^{3-}/-C ≡ N and C=N–C bonds. In addition, the high-resolution O1s spectra of the Ox-gCN exhibited two new spectra at approximately 530.2 eV and 531.9 eV (Fig. S4(b)), indicating the formation of –C=O and C–OH bound to the g-CN framework due to the sulfuric acid oxidation for 60 min [25]. The percentage of C–OH and –C=O in Ox-gCN was calculated to be 21.43 At.% and 8.97 At.%. In bulk g-CN, a narrow peak at 530.2 eV was observed for -C=O, with a bond percentage of 18.77 At.%. Interestingly, the integrated C–OH area ratio in Ox-gCN ($A_{C\text{-}OH} = 0.17$) was significantly higher than that of bulk g-CN, suggesting that sulfuric acid oxidation increased the amount of oxygen functional groups, especially the hydroxyl groups on the surface [22,25–29]. Additionally, the high-resolution S2p$_{(3/2)}$ spectra of Ox-gCN (Fig. S4(d)) showed a smaller amount of sulfonate (-SO₃H) functionalization at 167.1 eV due to sulfuric acid oxidation, which is absent in bulk g-CN (Fig. S4(d)) [30]. We successfully modified pure g-CN into Ox-gCN, which was mainly composed of –C=O and C–OH groups on its surface.

The optical properties of bulk g-CN and Ox-gCN were investigated using UV–Vis and photoluminescence (PL) spectroscopy. As shown in Fig. S5(a), pure g-CN and Ox-gCN exhibit emission peaks at approximately 437 and 406 nm, respectively, upon excitation at 375 and 322 nm, respectively. The blue shift of Ox-gCN is probably due to oxygen functionalization and surface defects during sulfuric acid oxidation [31–33]. The PL excitation-dependent emission spectra of g-CN and Ox-gCN showed similar fluorescence emissions in the 400–600 nm range, indicating a negligible change in the optical properties of Ox-gCN (Figs. S5(b and c)).
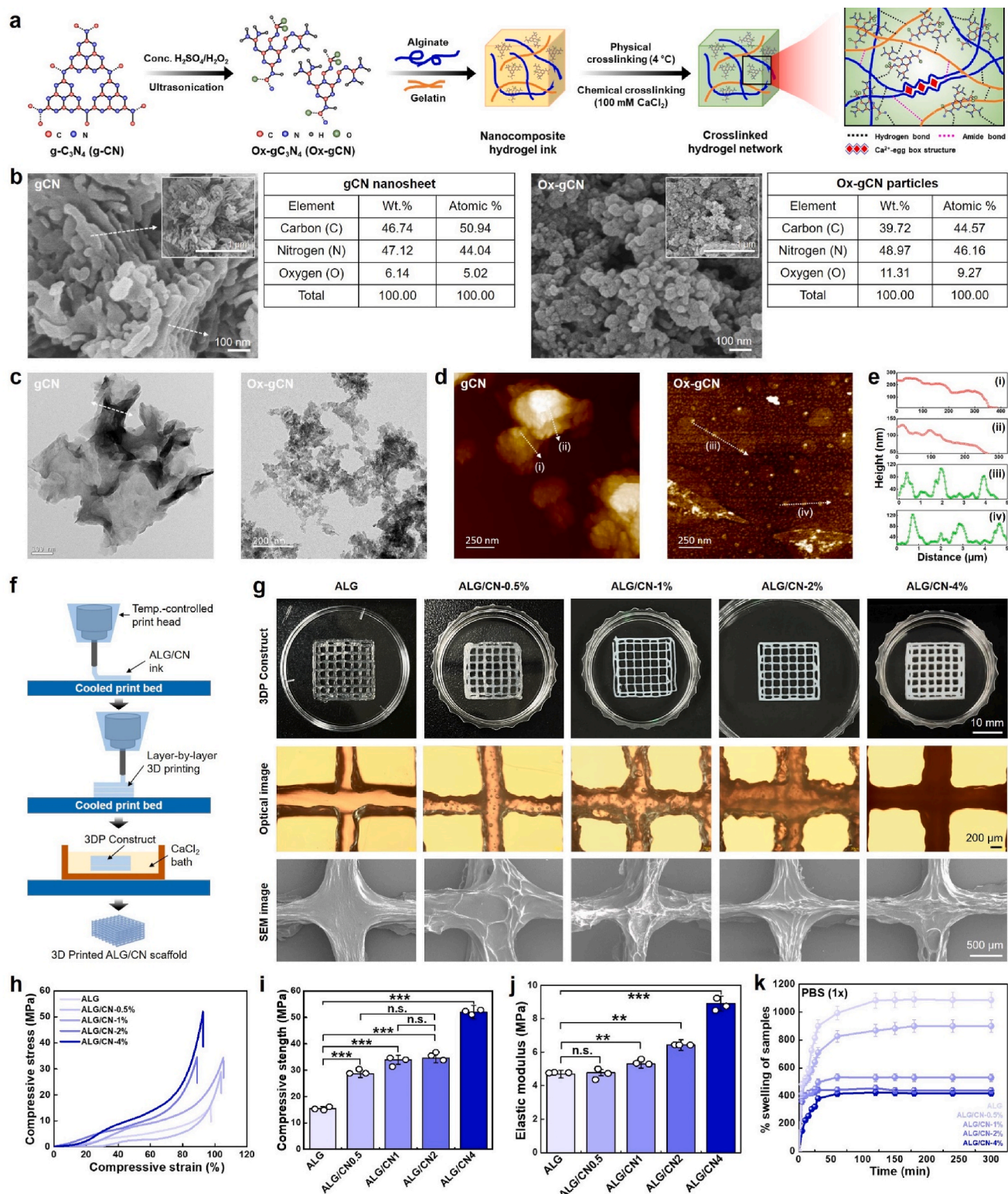
Fig. 1. Characterization of the 3D printed photocatalytic nano/biocomposite scaffolds. **(a)** Schematic illustration of the g-CN and Ox-gCN synthesis and the hydrogel fabrication procedure with possible interactions. **(b)** FE-SEM morphology of the as-synthesized g-CN and Ox-gCN with corresponding EDS mapping images showing the oxygen functionalization. Scale bar: 100 and 500 nm. **(c)** HR-TEM images of the as-prepared g-CN and Ox-gCN. Scale bar: 200 and 500 nm. **(d, e)** AFM phase and 3D topographical images of the as-prepared g-CN and Ox-gCN. Scale bar: 250 nm. **(f)** Schematic illustration of the 3D printing process of the ALG/CN hydrogel ink. **(g)** Digital, optical, and FE-SEM images of the 3D printed scaffolds containing Ox-gCN (0–4 wt%). The displayed images correspond to the printed strand and cross-connecting junctions. Scale bar: 200 μm, 500 μm, and 10 mm. **(h–j)** Compressive stress-strain curve with corresponding strength and elastic modulus of the pure ALG and its nanobiocomposite scaffolds. Data reported as mean ± s.d. of triplicated ($n = 3$) experiments, with statistical significance at **$p < 0.01$ and ***$p < 0.001$ (One-way ANOVA). **(k)** Swelling efficiency of the ALG and its composite scaffolds in PBS at indicated time points.

4

2.2. Spectroscopic characterization of the 3D-printed scaffolds

Using a cooled print head and bed, the nano/biocomposite hydrogels were extruded using a direct ink writing (DIW) 3D printer. The extrusion pressure was set to 120 kPa for all composites. The digital, optical, and FE-SEM images of the micromorphologies of pure ALG and its nanocomposite scaffolds are shown in Fig. 1(d). Interestingly, the pure ALG scaffold had a smooth morphology, whereas the nanocomposites displayed a wavy to flaky morphology as the concentration of Ox-gCN increased from 0.5 to 4 wt%. The scaffolds were crosslinked with 100 mM $CaCl_2$, which allowed chemical crosslinking between the ALG-alginate and alginate-gelatin frameworks, resulting in a tougher hydrogel matrix. Fig. 1(e) shows the SEM images with the corresponding EDS maps of pure ALG and its nanocomposite scaffold showing the Ca distribution. The chemical interactions between ALG and Ox-gCN were investigated using FT-IR spectroscopy (Fig. S6). Pure ALG (alginate/gelatin hydrogel) exhibited two absorption peaks at approximately 1627 and 1545 cm^{-1}, corresponding to the interaction between alginate and gelatin via physical crosslinking and formation of amide bonds ($-CO-NH_2$). Additionally, the stretching vibrations at approximately 3267 cm^{-1} were attributed to hydroxyl (-OH) groups in the alginate and gelatin structures [3a]. Moreover, the stretching vibrations observed between 1200 and 910 cm^{-1} were attributed to the D-mannuronic acid and L-glucuronic acid backbones of alginate [51]. Interestingly, the absorption peak at approximately 1036 cm^{-1} in ALG, which is responsible for the stretching vibration of carbonyl and amine moieties, gradually shifted to 1029 cm^{-1} as the concentration of Ox-gCN increased from 0.5 to 4 wt% (ALG/CN-0.5 % → ALG/CN-4%), suggesting the interaction between Ox-gCN and ALG, respectively. The strong interaction between Ox-gCN and ALG is responsible for the wavy or flaky morphology of the ALG matrix during 3D printing, as presented in Fig. 1(f). The EDS mapping spectra of the ALG and ALG/CN-4% were recorded to evaluate the C, O, and Ca contents of the scaffold. As shown in Fig. 1(g), the C and O contents gradually increased by 49.67 wt% and 44.33 wt% after incorporating Ox-gCN. However, we observed a negligible change in the Ca content (8–9 wt.%) in both ALG and Alg/CN-4%, as $CaCl_2$ was used for hydrogel crosslinking.

The mechanical properties of the 3D-printed hydrogel scaffolds were evaluated using a uniaxial tensile machine (UTM) under compressive loading according to the American Society for Testing and Materials (ASTM-F2150) standards. As shown in Fig. 1(h), the compressive stress increased gradually as the concentration of Ox-gCN in the ALG matrix increased from 0.5 to 4 wt%. The enhanced compressive stress in the nanocomposite scaffolds was due to the increased interaction and physical crosslinking between ALG and Ox-gCN and/or Ca^{2+}, which facilitated viscous-to-elastic transition without damaging the polymer matrix. The hydroxyl and oxygen-containing functional groups in nanomaterials enhance the mechanical property of the polysaccharide/protein-based hydrogels by forming stronger hydrogen or amide bonds with the polymer chain [6,19,52]. The compressive strength of the freeze-dried ALG scaffold was 15.45 ± 2.58 MPa, which significantly (*$p < 0.05$) increased to 51.95 ± 0.88 MPa following incorporation of Ox-gCN (Alg/CN-4%) (Fig. 1(i)). Similarly, the elastic modulus of the scaffolds increased significantly (*$p < 0.05$) from 4.69 ± 1.27 MPa to 8.9 ± 1.78 MPa after Ox-gCN incorporation. However, compared with the ALG scaffold, no significant difference in elastic modulus was observed between the ALG/CN-0.5 % (3.96 MPa) and ALG/CN-1% (4.89 MPa) (Fig. 1(j)), which could be attributed to the stretching or partial breaking of the polymer matrix. Consistent with previous studies, these results suggest that improvement in mechanical strength of the formulated hydrogel inks was primarily due to the reinforcement of the 2D Ox-gCN nanoparticles.

The wettability of the developed hydrogel scaffolds was investigated through a swelling test in phosphate-buffered saline (PBS) for 300 min at room temperature under gentle shaking, and the results are illustrated in Fig. 1(k). The scaffold's porosity and swelling are essential for cell adhesion, proliferation, and differentiation [4]. Reduced swelling may hinder nutrient exchange and oxygen diffusion, resulting in cell death [53]. Moreover, the oxygen-containing self-catalytic scaffolds with reduced porosity may promote cell proliferation and differentiation through continuous oxygen/nutrient exchange to the culture cells and induce bone regeneration potential [54]. Compared with the ALG/CN scaffolds, the pure ALG scaffold exhibited greater swelling efficiency within 300 min incubation. In addition, all the hydrogel scaffolds exhibited saturation swelling at approximately 50–60 min of incubation in PBS, indicating hydrophilicity, which could be attributed to the bulk porosity of the samples. We observed a gradual decrease in the porosity with increasing Ox-gCN content. The porosity of the ALG, ALG/CN-0.5 %, ALG/CN-1%, ALG/CN-2%, and ALG/CN-4% were 54.77 ± 1.34 %, 51.48 ± 0.55 %, 46.28 ± 2.11 %, 35.04 ± 0.22 %, and 33.87 ± 1.44 %, respectively. The highly inner-connected polymer network and dense packing of Ox-gCN resulted in decreased porosity and swelling efficiency as the Ox-gCN content increased from ALG to ALG/CN-4%. This trend was also reflected in the degradation behavior of the 3D-printed scaffolds after 21 days of incubation in PBS. As shown in Fig. S7, the degradation potential of the nanocomposite scaffolds decreased slightly with increasing Ox-gCN content (0.5–4 wt.%). The pure ALG scaffold exhibited the highest degradation rate at approximately 45.96 ± 2.1 % after 21 days. The degradation rates of ALG/CN-0.5 %, ALG/CN-1%, ALG/CN-2%, and ALG/CN-4% scaffolds were 43.2 ± 3.24 %, 37.14 ± 0.8 %, 29.41 ± 1.6 %, and 22.93 ± 1.55 %, respectively. Therefore, this controlled and gradual degradation of the ALG/CN scaffolds suggests their suitability for long-term bone regeneration study *in vivo*.

2.3. Viscoelastic and printing properties of the nano/biocomposite hydrogels

The viscoelastic and shear-thinning behavior of the fabricated nano/biocomposite inks was evaluated using a rotational rheometer under varying amplitude (strain%) and frequency (ω, Rad/s) sweeps at 25 °C. As shown in Fig. 2(a), the pure ALG and its nanocomposite hydrogels exhibited a strain-dependent change in storage modulus (G′) and loss modulus (G″) over a stain range of 0.1–1000 %. G′ values increased with increasing concentrations of Ox-gCN from 0.5 to 4 wt%. All the hydrogels exhibited a yield point at approximately 100 % strain, indicating an elastic to viscous transition. The change in the shear stress under varying strains is shown in Fig. 2(b). This was also reflected in the change of complex viscosity (η*) of the hydrogels under varying strain conditions. As shown in Fig. 2(c), the fabricated hydrogels showed higher viscosity at low shear strain (0.1 %); however, viscosity significantly decreased when the strain rate increased from 0.1 to 1000 %. To further understand the role of the nanofiller (Ox-gCN) in improving the hydrogel stability, we evaluated hydrogel viscoelasticity under varying frequencies. As shown in Fig. 2(d), the fabricated hydrogels displayed a frequency-dependent change in G′ and G″ values. The control hydrogel (ALG) exhibited negligible change in G′, whereas the nanocomposite hydrogels showed increased G′ values with increasing frequency from 0.1 to 100 Rad/s, reflecting their viscoelastic nature. Incorporating Ox-gCN (nanofiller) restricted the polymer motion at higher frequencies and amplitudes owing to greater interaction with the ALG backbone and tight packing with chemical crosslinking. This trend was also evident in the complex viscosity (η*) under varying frequencies. As shown in Fig. 2 (e), the fabricated hydrogels displayed a frequency-dependent change in viscosity, with higher viscosity observed at low frequency (0.1 Rad/s) region and lower viscosity observed at higher frequency (100 Rad/s) region, suggesting the shear-induced elastic-to-viscous transition, which is crucial for 3D printing applications. 3D printable inks must exhibit shear-thinning and thickening properties during 3D printing. The excellent printability and shear-thinning properties of alginate/gelatin or gelatin-based hydrogels under varying temperatures or printing pressure have been previously reported [4,55,56]. The shear-thinning property of the fabricated hydrogels was evaluated by measuring the
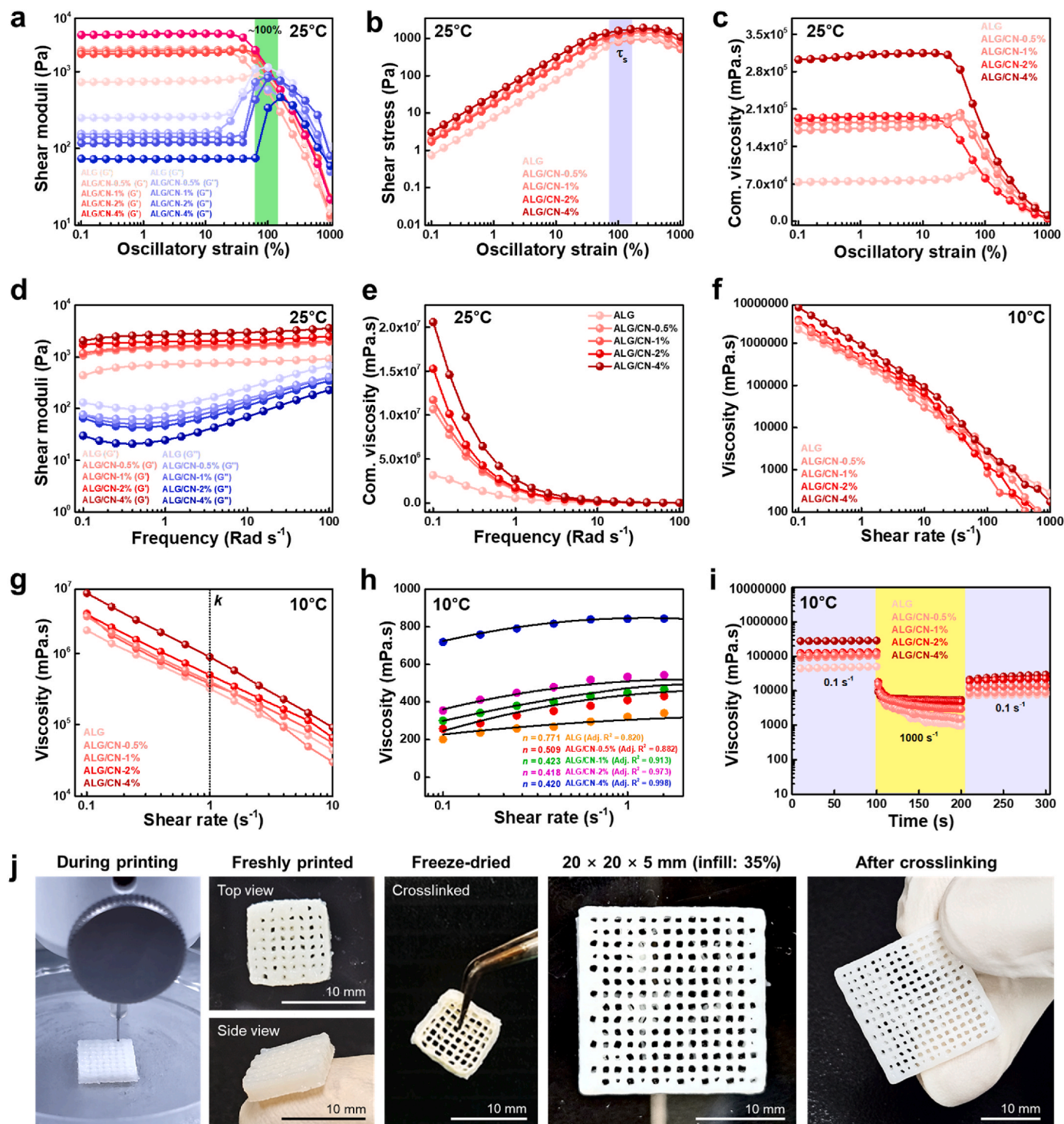
Fig. 2. Rheological investigation of the developed nanobiocomposite hydrogel inks. **(a)** The amplitude sweep test of the hydrogel inks at 25 °C shows the change in storage (G′) and loss modulus (G″) within a range of 0.1–1000 % strain. **(b)** Representative oscillatory strain vs. shear stress analysis of the hydrogel inks at 25 °C. **(c)** Representative complex viscosity (η^*) measurement of the hydrogels within a strain range of 0.1–1000 %. **(d)** The frequency sweep test of the developed hydrogel inks is within a range of 0.1–100 Rad/s at 25 °C. **(e)** Representative complex viscosity (η^*) measurement of the hydrogels within a frequency range of 0.1–100 Rad/s. **(f)** The flow curve (viscosity vs. shear rate) of the developed hydrogel inks at 10 °C. **(g)** The viscosity of the developed hydrogels at a shear rate 1/s. **(h)** Calculation and fitting of flow curve using Herschel-Bulkley fluid flow model at 1/s shear rate. Inset is the shear-thinning index (n) calculated for each hydrogel ink. **(i)** Representative thixotropic behavior of the hydrogel inks within a 0–300 s time frame at varying shear rates. **(j)** Digital photographs of the 3D printing process, chemical crosslinking, and stability testing of the 3D printed ALG/CN hydrogels. Scale bar: 10 mm.

flow curve, i.e., the change in viscosity under varying shear rates (0.1–100/s), and the results are shown in Fig. 2(f-h). The Ostwald-de Waele and the Herschel–Bulkley flow models are the commonly used mathematical models to describe ideal shear-thinning behavior in

hydrogels [55]. As shown in Fig. 2(f), the fabricated nano/biocomposite hydrogels displayed superior shear-thinning properties within a shear rate of 0.1–100/s at 10 °C. Moreover, the Herschel–Bulkley fitting of the hydrogel viscosity at a shear rate of 1/s demonstrated that all hydrogels

6

exhibited a shear-thinning index (n) < 1 (Fig. 2(g and h)). The values of n for ALG, ALG/CN-0.5 %, ALG/CN-1%, ALG/CN-2%, and ALG/CN-4% were 0.771, 0.509, 0.423, 0.418, and 0.420, respectively. The thixotropic behavior of the developed hydrogels was assessed by monitoring viscosity changes over time under varying shear rates up to 300 s, where the initial shear rate was 0.1/s, followed by high shear (1000/s) and low shear (0.1/s), and the results are shown in Fig. 2(i). The pure ALG hydrogel exhibited viscosities of approximately 46867.47 Pa (first interval), 966.25 Pa (second interval), and 6571.44 Pa (third interval). In contrast, the ALG/CN composites exhibited higher recovery rates as the concentration of Ox-gCN increased from 0.5 to 4 wt%. The ALG/CN-4% hydrogel exhibited viscosities of 289838.42 Pa (0.1/s), 6571.44 Pa (1000/s), and 35518.83 Pa (0.1/s), which were substantially higher than those of ALG. The gradual increase in the recovery strength after Ox-gCN reinforcement underscores its positive role in maintaining mechanical strength. Taken together, these results suggest that the fabricated hydrogels exhibited superior shear-thinning behavior with stress-yielding properties, which could benefit the 3D printing of biomimetic architectures.

Based on the rheological data, we tested the printing performance of the ALG/CN-1% hydrogel inks using $10 \times 10 \times 5$ mm^3 and $20 \times 20 \times 5$ mm^3 structures. Fig. 2(j) and Video S1 show an overview of the 3D printing process of ALG/CN-1% hydrogel ink, its chemical crosslinking, and its physical morphology after 3D printing. The layer-wise printing process is shown in Fig. S8(a). After 3D printing and desirable crosslinking, the hydrogels were freeze-dried to evaluate the strand thickness. The average strand thickness for the ALG/CN-1% scaffold was 62 ± 4.54 μm (Fig. S8(b)), which was comparable to that of the theoretical design. The 3D-printed ALG and ALG/CN-1% hydrogel scaffolds were used for the *in vitro* and *in vivo* experiments because of their exceptional biocompatibility, unless stated otherwise.

2.4. In vitro biocompatibility and osteogenic differentiation potential

The *in vitro* biocompatibility and morphology of hBMSCs in the presence of the fabricated hydrogels were assessed using live/dead, WST-8, F-actin, and H&E staining assays. The hBMSCs were cultured with the fabricated hydrogels for the desired time, and cytotoxicity levels were evaluated. As shown in Fig. 3(a), the hBMSCs adhered well to the hydrogel strands and exhibited a flattened morphology after 24 h of incubation. The WST-8 assay results demonstrated higher cell viability in the presence of hydrogel scaffolds than in the control group (Fig. 3(b)). The cell viability was significantly increased in the presence of ALG/CN-0.5 % (**$p < 0.01$) and ALG/CN-1% (**$p < 0.01$) than in other treated groups after 5 days, suggesting that the ALG/CN-1% formulation was non-toxic to hBMSCs. Additionally, a non-significant decrease in the viability of hBMSCs was observed with ALG/CN-4% scaffold after 5 days of incubation. The increased viability of hBMSCs in the presence of Ox-gCN could be attributed to the smaller size and greater solubility in the hydrogel matrix, which could be utilized as a source of fuel for mitochondrial activity [36–40]. Based on these results, a micro-scale bone model was 3D printed using Alg/CN-1% hydrogels to evaluate the hBMSCs infiltration and colony formation. Fig. 3(c) demonstrates the robust growth and viability of hBMSCs on the biomimetic microscale bone model, confirming the biocompatibility of Ox-gCN-reinforced hydrogels. To observe the actin morphology of the cultured hBMSCs, we stained them with an F-actin probe after 3 days of culture (Fig. 3(d)). A plate without any scaffold was used as the control. Interestingly, the hBMSCs exhibited distinct morphological changes as the concentration of Ox-gCN increased from 0.5 to 4 wt%. The F-actin anisotropy index further suggests that F-actin alignment was significantly higher in ALG/CN-1% (***$p < 0.001$) and Alg/CN-2% (***$p < 0.001$) than in control and other groups (Fig. 3(e)). The infiltration of hBMSCs within the hydrogel scaffold was also assessed by hematoxylin and eosin (H&E) staining after 7 d of incubation, and the results are shown in Fig. 3(f). Interestingly, the number of infiltrating cells was

higher in the ALG/CN-1% group than in the ALG group after 3 and 7 days of culture, which could be attributed to the good hydrophilic nature of the ALG/CN-1% hydrogel, higher availability of oxygen-containing groups in the presence of Ox-gCN, and viscoelastic nature of the hydrogel, which substantially contributed to hBMSCs proliferation, migration, and improved nutrient exchange [57–61].

The *in vitro* osteogenic differentiation capabilities of the ALG and ALG/CN-1% hydrogel scaffolds were evaluated using Alizarin Red S (ARS) and immunocytochemistry (ICC) staining methods. Prior to this, the osteogenic differentiation potential of bulk Ox-gCN (1 wt%) in hBMSCs was evaluated using ARS staining. The results are presented in Fig. S9(a). Notably, Ox-gCN treatment significantly (***$p < 0.001$) enhanced mineral deposition than in the control group after 14 days of incubation. Tiwari et al. [36] reported that red-light-absorbing g-CN nanosheets enhanced osteogenic differentiation of hBMSCs, which is consistent with our findings. A quantitative analysis of mineralization is shown in Fig. S9(b). Based on this, we selected 1 % Ox-gCN-containing hydrogel (*i.e.*, ALG/CN-1%) for investigating the osteogenic differentiation of hBMSCs. After 7 days of osteogenic induction, the ALG and ALG/CN-1% hydrogel groups exhibited minimal mineralized nodule formation, which substantially increased after 14 days of incubation. To validate this finding, the expression of the key osteogenic biomarker (Runx2) was assessed by ICC after 7 days of osteogenic differentiation. As shown in Fig. S10(a), both the ALG-and ALG/CN-1%-treated groups exhibited Runx2$^+$ hBMSCs adhering to the scaffold surfaces. Interestingly, the number of Runx2$^+$ cells was significantly (**$p < 0.01$) higher in ALG/CN-1%-treated groups than in ALG groups (Fig. S10(b)), highlighting the superior osteogenic potential of ALG/CN-1% with oxygen-containing Ox-gCN flakes.

2.5. Effects of ALG/CN on macrophages and osteo-immunomodulation

The viability and bioactivity of RAW 264.7 cells in the presence of the ALG/CN scaffold were investigated using the WST-8 assay and screening of inflammatory proteins and gene markers after 24 h of incubation. For classical activation [62], LPS (200 ng/mL) and serum-free DMEM were used as the positive and negative controls, respectively. Initially, macrophages were cultured on the 3D-printed scaffolds to observe the impact of the scaffolds on cell proliferation. The ALG/CN-1% composite exhibited a significant (*$p < 0.05$) abundance of viable clusters after live/dead staining, as depicted in Figs. S11(a and b). Subsequently, the macrophage cell viability was assessed on days 1, 3, and 5. ALG/CN-1% demonstrated optimal cell viability, which was significantly higher (**$p < 0.01$) than in the control group after 5 days, as indicated in Fig. S11(c). In the ALG/CN-2% and ALG/CN-4%, a negligible change in viability of RAW 264.7 cells was observed on day 1. However, on day 5, the RAW 264.7 cells viability was significantly (**$p < 0.01$) decreased in the ALG/CN-4% group than in the control group, suggesting that higher concentrations (4 wt%) of Ox-gCN was not suitable for RAW 264.7 cells. The cytotoxicity of RAW 264.7 cells in the presence of 4 wt% Ox-gCN could be attributed to the lower swelling efficiency of the ALG/CN-4% scaffolds, which inhibited the adhesion and proliferation of the cells. These findings highlight ALG/CN-1% as the most biocompatible scaffold, making it the preferred choice for polarization studies. Next, we evaluated the morphology of adherent RAW 264.7 cells on the surface of the 3D scaffold. As shown in Fig. S11(d), the several F-actin-stained colonies of RAW 264.7 cells were clearly visible on the ALG/CN-1% scaffold, suggesting its proliferative and adhesive nature.

Subsequently, we examined the phenotypic changes in RAW 264.7 cells in the presence of ALG/CN-1% scaffolds after incubation for 24 h. ICC staining (Fig. 4(a and b)) revealed differential expression of the iNOS/CD163 marker in macrophages. Notably, LPS (positive control) treatment significantly increased (****$p < 0.0001$) the cytoplasmic iNOS expression (iNOS$^+$ cells) after 24 h (Fig. S12(a)), indicating classical activation [63]. Additionally, iNOS$^+$ cells were significantly (***p
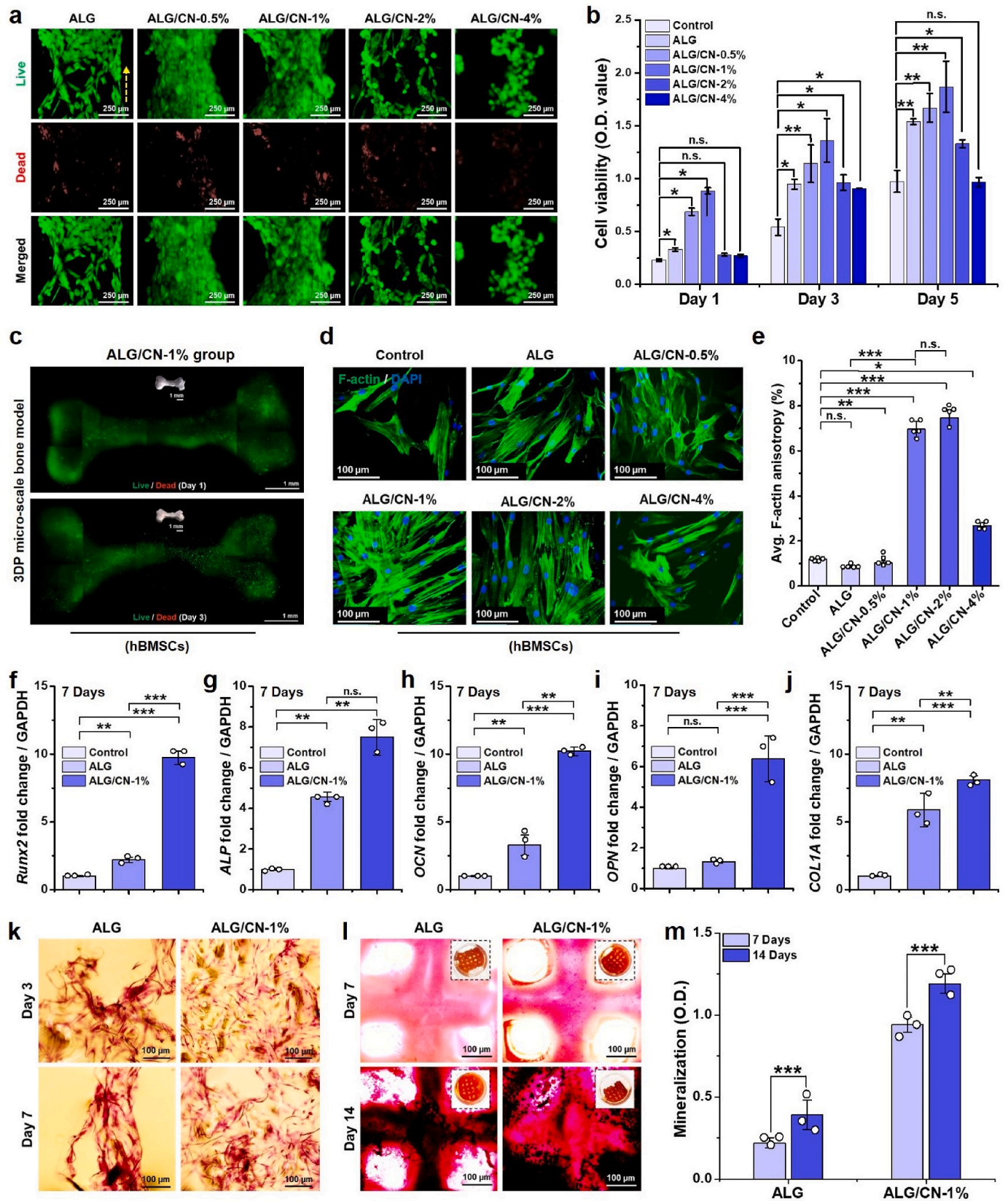
(caption on next page)

Fig. 3. *In vitro* biocompatibility and osteogenic differentiation potential of hBMSCs. **(a)** Representative live/dead staining images of hBMSCs growing onto the 3D-printed hydrogel strands. The images were taken after 24 h of incubation in DMEM media. Scale bar: 250 μm. **(b)** WST-8 cell viability assay of hBMSCs in the presence of 3D printed hydrogels at indicated time points. Data reported as mean ± s.d. of triplicated ($n = 3$) experiments, with statistical significance at *$p < 0.05$ and **$p < 0.01$ (One-way ANOVA). **(c)** Reconstructed live/dead staining images of hBMSCs growing onto the 3D printed micro-scale bone model with Alg/CN-1% inks. Scale bar: 1 mm. **(d)** Representative FL images of hBMSCs showing the F-actin morphology in the presence of 3D printed hydrogels after 3 days of culture. **(e)** Quantification of F-actin anisotropy index (%) of the hBMSCs in various treatment groups after 3 days of incubation. At least 5 independent images were accessed through ImageJ (v1.8) software to access the actin anisotropy. Statistical significance was considered at *$p < 0.05$, **$p < 0.01$, and ***$p < 0.001$ (One-way ANOVA). **(f–j)** qRT-PCR results show the expression of osteogenic marker genes in hBMSCs after 7 days in the presence of fabricated scaffolds. **(k)** Representative H&E staining images of the hBMSCs showing the cellular infiltration inside the Alg and ALG/CN-1% scaffolds after 7 days of culture. Scale bar: 100 μm. **(l, m)** Alizarin Red-S (ARS) staining images with quantitative data of the 3D printed scaffolds showing the mineral deposition after 7 and 14 days of incubation in osteogenic differentiation media. Scale bar: 100 μm. (For interpretation of the references to color in this figure legend, the reader is referred to the Web version of this article.)

< 0.001) decreased in ALG and ALG/CN-1% scaffold-treated groups than in the LPS group, suggesting attenuated iNOS expression. In contrast, CD163 expression showed an inverse trend, with a significant increase in CD163+ cells in ALG-(***$p < 0.001$) and ALG/CN-1%--treated groups (***$p < 0.001$) than in the LPS group (Fig. S12(b)), suggesting that incorporation of Ox-gCN into the ALG matrix enhances CD163 expression. No significant change in CD163 expression was observed in the control group compared with that in the LPS group. The calculated ratio for M2/M1 polarization was highest in the ALG/CN-1%-treated samples (Fig. S12(c)), suggesting its polarization potential. Furthermore, the number of elongated cells was significantly higher (***$p < 0.001$) in ALG/CN-1%-treated groups than in the control and other groups (Fig. S12(d)).

To verify the phenotypic changes in macrophages, quantitative real-time reverse-transcription polymerase chain reaction (qRT-PCR) analysis of major gene markers (*IL-6*, *TNF-α*, and iNOS, Arg-1, *TGF-β*, and *VEGF*) was performed after 24 h of cell culture (Fig. 4(c)). Interestingly, the qRT-PCR results show that the ALG and ALG/CN-1% scaffolds significantly upregulated the expression of *Arg-1* (fold change >8.0, ***$p < 0.001$), *TGF-β* (fold change >10.0, ***$p < 0.001$), and *VEGF* (fold change >10.0, ***$p < 0.001$) gene markers, while downregulating the expression of *IL-6* (fold change <5.0, ***$p < 0.001$), *TNF-α* (fold change <4.0, ***$p < 0.001$), and *iNOS* (fold change <3.0, *$p < 0.05$ and ***$p < 0.001$) markers than in the control and LPS-treated groups. The LPS (200 ng/mL)-treated groups exhibited higher *TNF-α* expression than in the control and other groups, indicating inflammatory activation of macrophages. These results aligned with the ICC data, highlighting the superior immunomodulatory effects of 3D-printed ALG/CN-1% scaffold on RAW 264.7 cells, which would be beneficial for inducing immuno-modulatory bone regeneration. Owing to the visible-light responsive properties of the Ox-gCN, we further evaluated the effect of light-irradiation time (0.5, 2, 5, and 10 min, 100 W Xe lamp) on macro-phage polarization using ALG/CN-1% scaffold. The experiment was conducted by evaluating their cytokine profiles using a Raybiotech® mouse cytokine array. Besides, the macrophage without any light exposure was considered as the control group. As depicted in Fig. 4(d), the light-irradiation time significantly changed the cytokine/chemokine expression in RAW 264.7 cells. We observed a slight increase in the secretion of pro-inflammatory cytokines (IL-1β, IL-6, and TNF-α) in 0.5 min of light irradiation, while an enhancement of anti-inflammatory cytokines (IL-4, IL-10, and VEGF-A) after 2–10 min exposure. The initial 30s (=0.5 min) light exposure through ALG/CN-1% scaffold activated the phagocytotic nature of RAW 264.7 cells (M1 state), which is primarily associated with foreign-body reaction [82]. However, long-time light irradiation (2–10 min) gradually activated the voltage-gated ion channels in RAW 264.7 cells, resulting in the activation of the M2 phenotype [82,83]. Thus, the quiescent (=short time) M1 and prolonged M2 polarization upon visible-light exposure are helpful for eradicating pathogenic attack during injuries, while long-term M2 polarization will sustain tissue healing.

To assess osteo-immunomodulation, hBMSCs were exposed to a macrophage-conditioned medium (M-CM) extracted from the RAW 264.7 cell supernatant for 14 days. The impact of scaffold M-CM on the osteogenic induction of hBMSCs and its possible underlying mechanisms

were studied using ARS staining, phosphorylation array, and ALP staining. Notably, ALG/CN-1% (M-CM) supplementation enhanced mineralized nodule formation after 7 and 14 days due to the presence of various inflammatory cytokines and chemokines in the M-CM via paracrine signaling (Fig. 4(e)). The ARS+ staining area was significantly increased (***$p < 0.001$) in the ALG/CN-1% (M-CM)-treated groups than in the control (M-CM) and ALG (M-CM)-treated groups (Fig. 4(f)), suggesting the potential role of ALG/CN-1% scaffold in osteo-immunomodulation. Subsequently, the M-CM-treated hBMSCs were analyzed for the expression of key phosphorylating proteins within 7 days of immunomodulation using a Raybiotech® human phosphoryla-tion pathway profiling array. As shown in Fig. 4(g), the expression of signaling proteins for hBMSCs was observed in all groups related to pERK-1 (P-tyrosine-202/204), pERK-2 (P-tyrosine-185/187), pMKK3 (P-serine-189), p38 (P-tyrosine-180/182), and p-JNK (tyrosine-183). Quantitative fold change values are presented in Fig. 4(h). Notably, p-ERK-1/2 and p38 expression were significantly upregulated following ALG/CN-1% (M-CM) treatment *in vitro*, suggesting the role of M-CM of M2-polarized macrophages in paracrine signaling of hBMSCs through the phosphorylation of tyrosine/serine residues of ERK and p38, which subsequently activate the Smad-1/3/5 transcription factor, resulting in enhanced expression of osteogenic transcription factors [64–66].

2.6. Photocatalytic antibacterial performance

The visible-light-driven photocatalytic properties of the Ox-gCN-containing scaffolds were evaluated to investigate their potential for bacterial biofilm eradication. The photocatalytic properties of 2D nanomaterials are mainly influenced by the number of photons absorbed and the separation efficiency of light-driven electron-hole pairs [34,35,46]. First, we investigated the photocatalytic effect of the Ox-gCN-containing scaffolds. The ALG/CN-1% scaffold was selected for photocatalytic studies because of its superior biological activity. The photocatalytic performance of the ALG/CN-1% was estimated *via* photo-degradation of RhB as the target molecule under visible light. Fig. S13(a) shows the gradual decrease in intensity of the characteristic absorption peak of RhB at 554 nm under visible light in the presence of the ALG/CN-1% scaffold. The insets show digital images of the time-dependent discoloration of RhB after photodegradation under daylight and UV illumination, respectively. Fig. S13(b) shows the con-centration decay profile (C/C_0) of RhB over time in the presence of the ALG/CN-1%. A blank experiment was performed to assess the self-decomposition of RhB under visible light, which demonstrated almost negligible degradation after 300 min of irradiation. In contrast, the presence of the photocatalyst facilitated enhanced degradation (94 %). Fig. S13(c) shows the plot of -ln (C/C_0) vs. time, which confirms that the degradation of RhB followed pseudo-first-order kinetics, with a degradation rate of 0.01 min^{-1}. To verify the underlying mechanism of photodegradation, EPR spectroscopy was performed to understand radical formation during catalysis. As shown in Figs. S13(d and e), the ALG/CN-1% scaffold can effectively produce singlet oxygen (• O$_2$) and hydroxyl radicals (• OH) under 100 W Xe lamp irradiation for 10 min compared to the dark condition, indicating the positive role of free radicals in photo-degradation of RhB [45–50]. Therefore, 10-min light
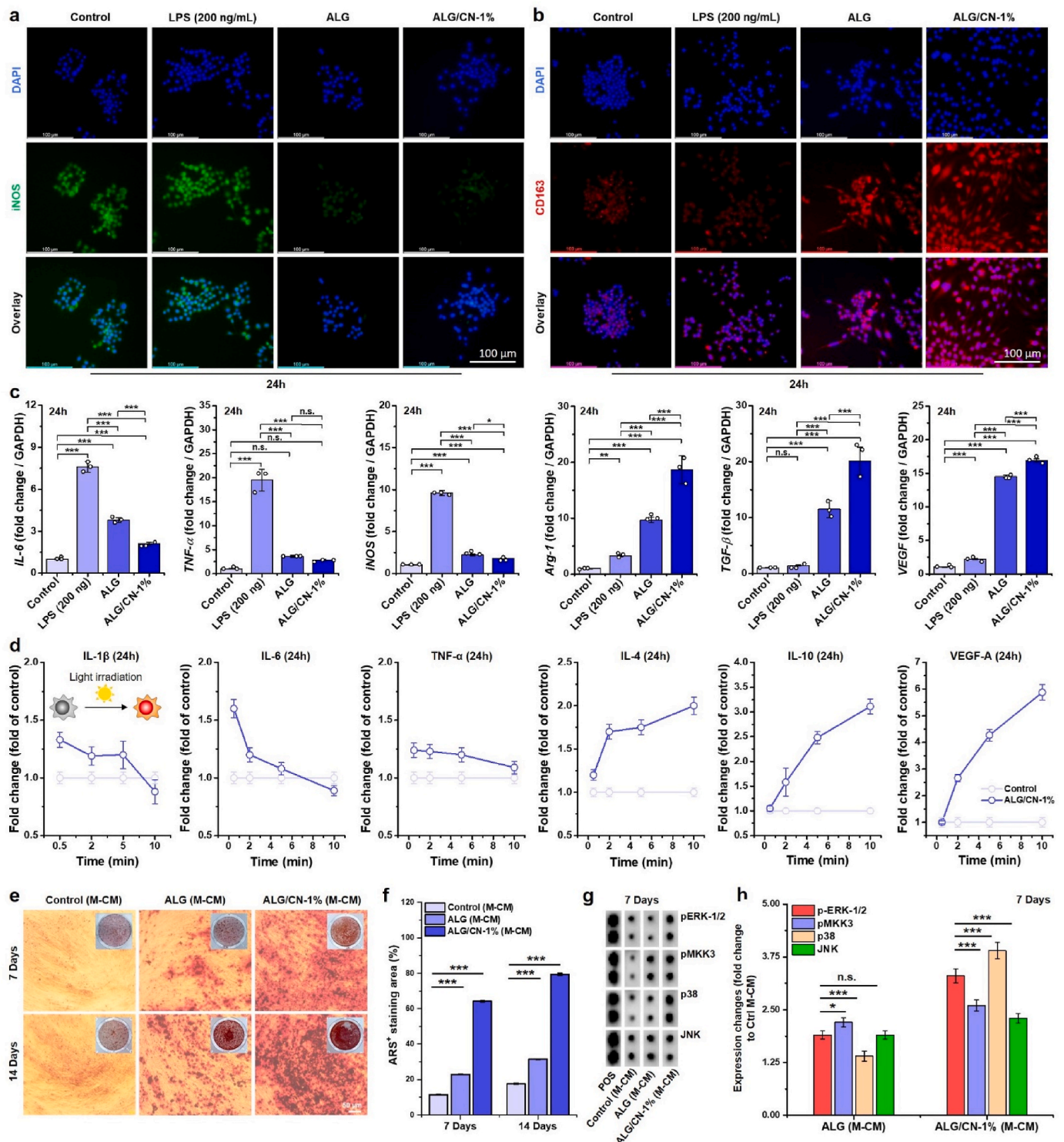
Fig. 4. Effect of ALG/CN scaffold and light irradiation on macrophage cells *in vitro*. **(a, b)** Representative FL microscopy images of RAW 264.7 cells showing the expression of iNOS and CD163 markers in various treatment groups after 24 h of incubation. LPS (200 ng/mL was taken as positive control). Scale bar: 100 μm. **(c)** qRT-PCR results of the RAW 264.7 cells showing the expression of gene markers (*IL-6, TNF-α, iNOS, Arg-1, TGF-β,* and *VEGF*) gene markers expression after 24 h of incubation. Data reported as mean ± s.d. of triplicated ($n = 3$) experiments, statistical significance at *$p < 0.05$, **$p < 0.01$, and ***$p < 0.001$ (One-way ANOVA). **(d)** Representative expression profiles of cytokines in macrophages after visible light irradiation (100 W Xe lamp) with ALG/CN-1% scaffolds at different times (0.5, 2, 5, and 10 min). Data was normalized to the control group and represented as fold change for each cytokine. **(e)** ARS staining images of the hBMSCs in the presence of M-CM at indicated time points. Scale bar: 50 μm. **(f)** Quantification of ARS data. **(g, h)** Raybiotech® mouse phosphorylation antibody array of sample groups with corresponding quantification data showing the activation of various signaling molecules. Data reported as mean ± s.d. of triplicated ($n = 3$) experiments, statistical significance at *$p < 0.05$, **$p < 0.01$, and ***$p < 0.001$ (One-way ANOVA).

10

treatment was selected for the antibacterial study.

To examine the effects of the ALG/CN-1% scaffold on visible-light-driven bacterial eradication and biofilm disruption, two common model bacteria, for example, *E. coli* (gram-negative) and *S. epidermidis* (gram-positive), were analyzed. Fig. 5(a and b) shows agar plate images depicting the growth of *E. coli* and *S. epidermidis* under two conditions: with (w/) and without (w/o) 100 W Xe irradiation. A digital photograph of the light-mediated experimental setup is shown in Fig. S13(f) and Video S2. Pure ALG scaffold and PBS were used as the positive and negative controls, respectively. In the absence of light irradiation, the colony-forming area of *E. coli* with 50 mg/mL of ALG and ALG/CN-1% hydrogel scaffolds was approximately 1.26 % and 0.89 %, respectively, compared to the control set of *E. coli* (1.4 %). A substantial bactericidal effect was detected within 10 min of Xe lamp irradiation in ALG/CN-1% group (0.04 %), indicating the potential bactericidal effects. The photocatalytic antibacterial activity had a greater impact against *S. epidermidis* following light irradiation. Quantitative results of the colony-forming areas of *E. coli* and *S. epidermidis* are presented in Fig. 5 (c).

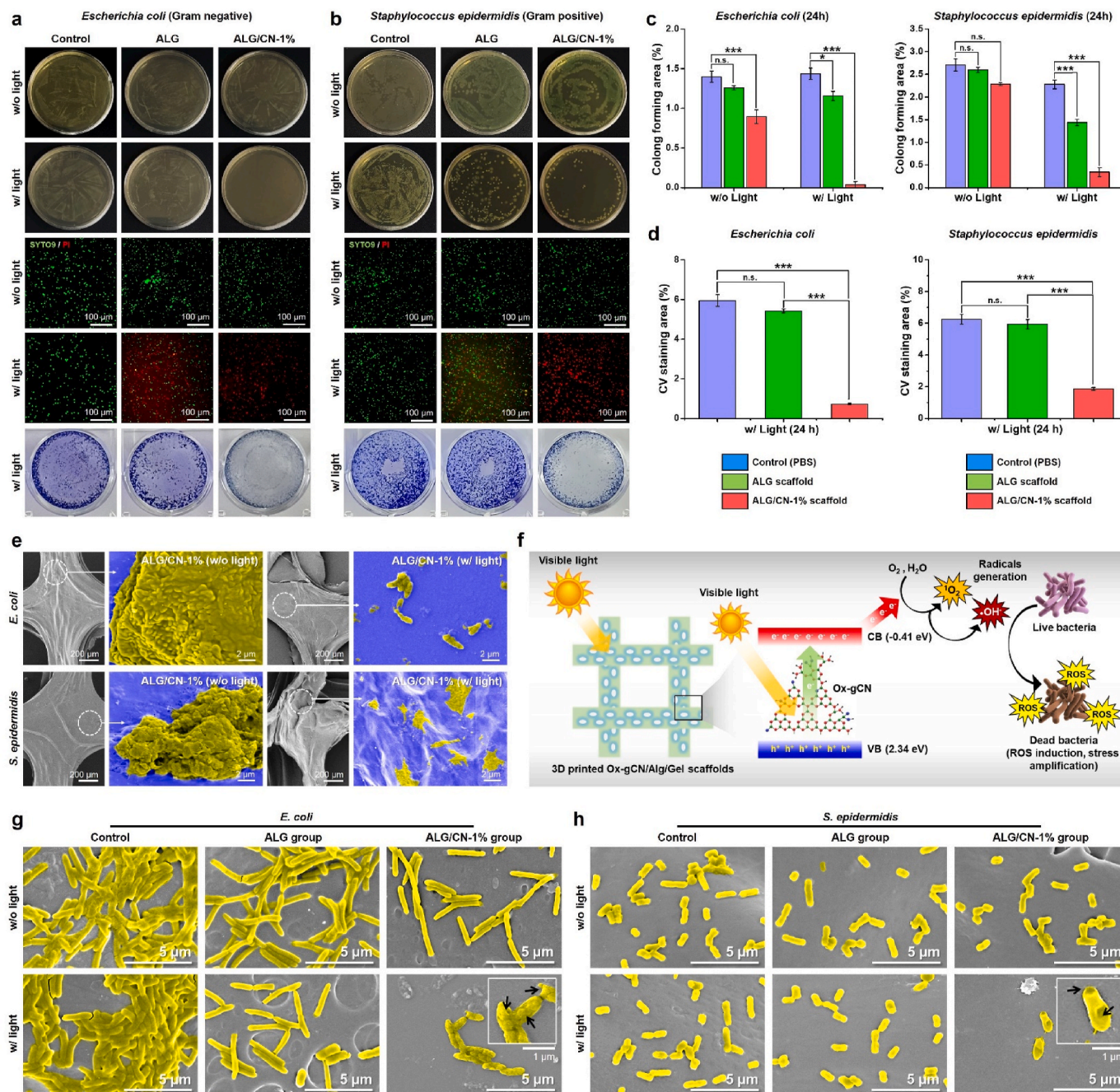The results of the SYTO9/PI (live/dead) staining were consistent

Fig. 5. Evaluation of the photocatalytic antibacterial performance of the ALG/CN scaffolds *in vitro*. **(a, b)** Representative plates of bacteria culture w/or w/o visible light treatment (100 W Xe lamp) for 10 min. Scale bar: 100 μm. **(c, d)** Quantification of the plate assay data. **(e)** The FE-SEM images showing the biofilm reduction test of the bacteria onto the scaffold surface. Scale bar: 2 and 200 μm. **(f)** Mechanisms of the visible-light-driven antibacterial therapy using composite scaffolds. **(g, h)** Morphological investigation of the bacteria (*E. coli* and *S. epidermidis*) killing process as evaluated by pseudo-color SEM. Insets are magnified images of damaged bacteria. Scale bar: 5 μm. Data reported as mean ± s.d. of triplicated ($n = 3$) experiments, with statistical significance at *$p < 0.05$ and ***$p < 0.001$ (One-way ANOVA). (For interpretation of the references to color in this figure legend, the reader is referred to the Web version of this article.)

with those obtained from the agar plate assay, indicating that the antibacterial activity of ALG/CN-1% was significantly enhanced in the presence of light irradiation. In the groups without light irradiation and the control groups, live cells were prominently visible, indicated by strong green fluorescence. In contrast, the red-stained cells indicated the presence of dead bacteria, which were more abundant in the ALG/CN-1%-treated groups following light irradiation. The visible light therapy enhanced the photocatalytic killing efficacy of the ALG/CN-1% scaffold against *E. coli* and *S. epidermidis* by the production of • O_2 and • OH radicals, as verified by EPR spectroscopy. Reactive oxygen species (ROS)

generation can inactivate bacteria by rupturing the cell membrane, damaging the DNA structure, inhibiting protein and metabolite synthesis, and enzyme inactivation [67]. Following exposure to visible light, the ALG/CN-1% scaffold facilitated • O_2 and • OH radical formation, promoting ROS amplification and subsequent degradation. This photocatalytic antibacterial effect using Ox-gCN has been previously reported [48,68,69].

The effect of ALG/CN-1% scaffold on biofilm destruction was further studied by examining the rupture of biofilms with or without light treatment. The biofilm used in this study was developed after 48 h of
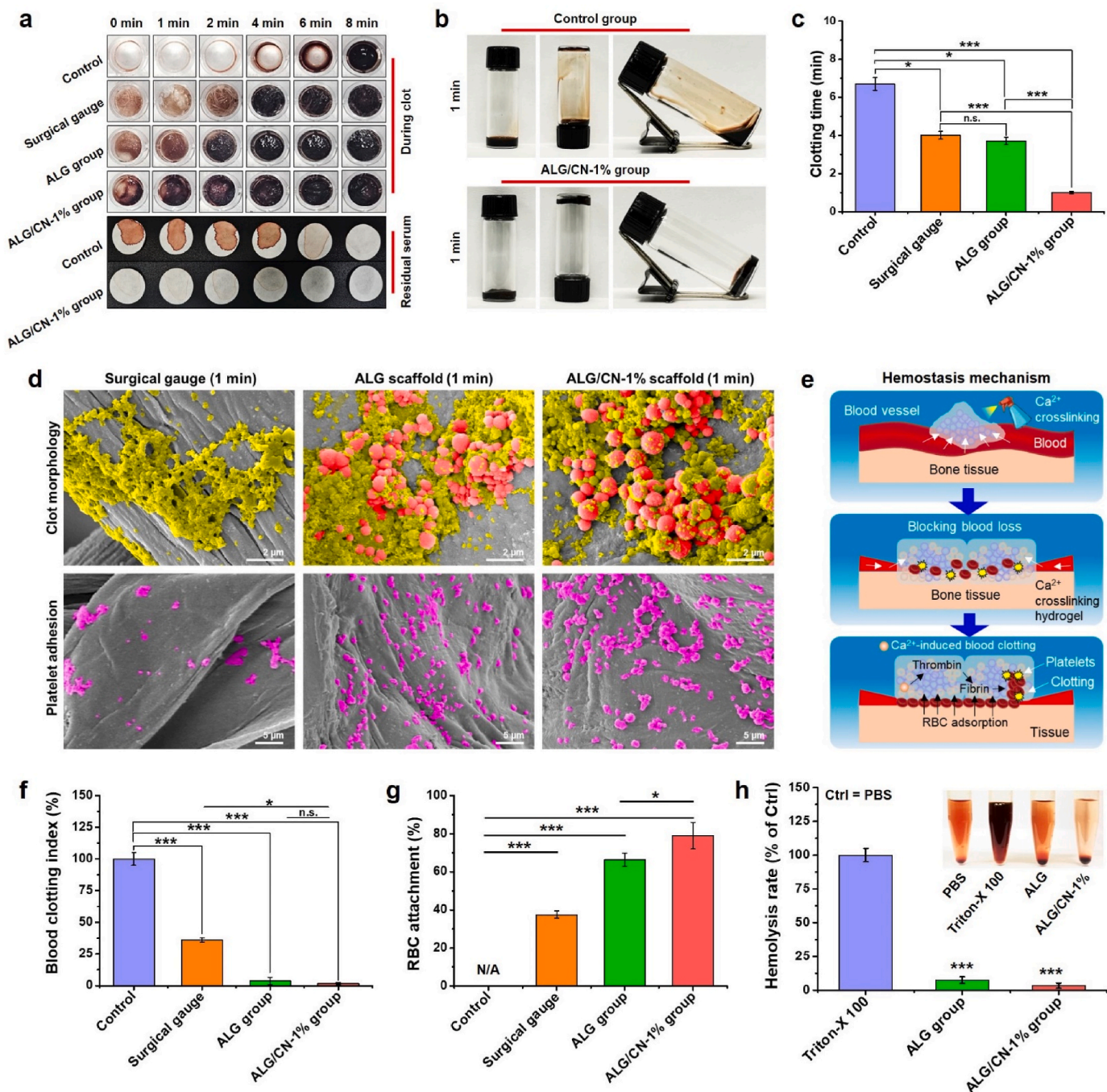

Fig. 6. *In vitro* hemostatic performance of the scaffolds. **(a)** Clotting time assay of the various formulations. **(b)** Digital images of the clotting time study by tube tilting method. **(c)** Quantification data of the clotting time assay. **(d)** FE-SEM observation for the clot morphology and platelet adhesion. Scale bar: 2 and 5 μm. **(e)** The mechanism of the hemostasis using the fabricated scaffolds. **(f, g)** Representative quantification data of the blood clotting index and RBC attachment study. N/A = No attachment. **(h)** Analysis of *ex vivo* hemolytic performance. Data reported as mean ± s.d. of triplicated (*n* = 3) experiments, statistical significance at *p < 0.05, **p < 0.01, and ***p < 0.001 (One-way ANOVA).

bacterial incubation. Biofilm disruption was evaluated using crystal violet (CV) staining, and the results are shown in Fig. 5(d). No significant difference was observed between the control and ALG-treated groups for both *E. coli* and *S. epidermidis*. However, the biofilm was significantly disrupted (***$p < 0.001$) when exposed to ALG/CN-1% within 10 min of Xe light irradiation. As shown in Fig. 5 (d), light exposure destroyed > 80 % of *E. coli* biofilms and 60 % of *S. epidermidis* biofilms. These results were verified using SEM images, as illustrated in Fig. 5(e). The light-irradiated ALG/CN-1% scaffolds had fewer adherent bacteria, which was consistent with CV staining. A schematic illustration of the photo-degradation of bacterial species and the ROS-induced killing mechanism is shown in Fig. 5(f).

The micromorphology of *E. coli* and *S. epidermidis* was further investigated to confirm the mechanisms of colony reduction and cytotoxicity. As shown in Fig. 5(g), viable bacteria preserved their cellular membrane integrity without visible light radiation w/or w/o scaffolds. However, when exposed to visible light phototherapy, membrane integrity was compromised, especially in ALG/CN-1% groups. Consequently, the photocatalytic activity of the ALG/CN-1% scaffold exhibited remarkable efficacy in neutralizing bacteria and attenuating biofilm development, which could be helpful in clinical applications, especially for managing post-surgical infections.

2.7. *In vitro hemostatic performance*

The surface morphology, functional groups, and wettability significantly affected the hemostatic performance of the hydrogel scaffold. Uncontrolled bleeding or blood loss during surgery are major concerns in bone replacement and bone tissue-related disorders [70,71]. Generally, hemostasis is associated with a series of biochemical and molecular events leading to clot formation via either intrinsic (damage response) or extrinsic (traumatic injury) pathways. Clotting factor X, plasminogen, prothrombin, and thrombin activation in response to damage or injury play key roles in blood clotting [72]. Biomaterials in contact with blood help absorb the blood and activate coagulation factors and blood cells. Therefore, the hemostatic properties of any biomaterial are evaluated by the number of adsorbed RBCs, platelets, and fibrin/thrombin production [72,73].

In this study, the hemostatic properties of the ALG and Alg/CN-1% scaffolds were evaluated by measuring the clotting time, blood clotting index (BCI), and RBC attachment assays. As shown in Fig. 6(a), the blood clotting time was monitored over 0–8 min using fresh mouse blood with a corresponding analysis of the residual plasma. A commercial surgical gauge was used as the positive control. Blood samples without any scaffold or gauge were used as negative controls. Digital photographs of the clot formation were also obtained using the tube-tilting method, as illustrated in Fig. 6(b). The control group without any scaffold showed delayed blood clotting, with an average time of 6.8 min. Blood clotting was relatively quicker with commercial gauge than in the control group (4.1 min, *$p < 0.05$). Notably, blood clotting occurred immediately (within 3 min of incubation at room temperature) in the ALG and ALG/CN-1% groups (*$p < 0.05$ and ***$p < 0.001$), underscoring their hemostatic potential. The observed clotting times for ALG and ALG/CN-1% were 3.4 and 1.7 min, respectively. Given that Ca^{2+} ions are crucial in hemostasis and wound healing, calcium-containing biomaterials may trigger platelet activation, followed by the activation of coagulation factor XIII, which ultimately triggers thrombin/fibrin formation [74, 75]. In this context, the ALG/CN-1% scaffold with oxygen-containing Ox-gCN facilitated increased capacity for binding Ca^{2+} ions in the polymer matrix, contributing to superior hemostasis, and could be particularly beneficial for treating bone-related hemorrhages during accidental injury. The quantitative data of the blood clotting time are shown in Fig. 6(c).

Microscopic clot formation was investigated by RBC/thrombin/fibrin clot formation and platelet adhesion after 1 min of incubation. Environmental field emission scanning electron microscopy (EF-SEM)

images shown in Fig. 6(d) reveal the clot morphology. For the surgical gauge, a small amount of thrombin/fibrin deposition was observed after 1 min. However, in the ALG and ALG/CN-1%-treated groups, a significant number of RBCs (red color) and thrombin/fibrin complexes (yellowish color) were observed, indicating their enhanced hemostatic potential. This finding was further confirmed by the platelet adhesion test using gauge and scaffolds, where the ALG and ALG/CN-1% scaffolds showed a significantly increased number of platelets than the commercial gauge, suggesting the role of Ca^{2+} ions in platelet adhesion and activation. A schematic illustration of the mechanism of ALG/CN-1% scaffold-assisted hemostasis is shown in Fig. 6(e).

To validate these findings, BCI (%) and RBC attachment tests were performed. The BCI is a time-dependent UV–Vis absorption-based test that measures untrapped RBCs from the clot. A higher absorption value of hemoglobin from the non-adhered RBCs indicates faster and superior hemostatic functionalities of the biomaterial scaffold [72]. The BCI value was measured by incubating freshly collected RBCs with scaffolds for 10 min and then recording the absorbance of the supernatant at 540 nm as a function of hemoglobin. As illustrated in Fig. 6(f), the BCI values were significantly higher for ALG and ALG/CN-1% scaffolds than for commercial gauge (***$p < 0.001$), indicating greater entrapment of RBCs in the clot. Additionally, the RBC attachment index (Fig. 6(g)) revealed that more than 60 % of RBCs adhered to ALG and ALG/CN-1% scaffolds, which was significantly (***$p < 0.001$) higher than control (0 %) and surgical gauge (38 %). Ca^{2+} crosslinking of alginate/gelatin matrix not only improves the ability of gelatin to adsorb RBCs and platelets but also activates the platelets to initiate coagulation process [81]. Moreover, increasing concentrations of Ox-gCN in ALG matrix considerably reduced porosity (ALG → ALG/CN-4%), which facilitated RBC capture and fibrin clot formation. These results indicate that the fabricated ALG/CN hydrogel scaffolds have tremendous potential for hemostasis by activating platelets, increasing the absorption rate of RBCs, and enhancing thrombin/fibrin complex formation, which is especially beneficial in traumatic bone regeneration.

The *ex vivo* blood biocompatibilities of the fabricated ALG and Alg/CN-1% scaffolds were assessed by hemolysis assay, and the results are shown in Fig. 6(h). Fresh RBC samples were incubated for 120 min at 37 °C, and 1 × PBS and Triton-X 100 were used as negative and positive control groups, respectively. Notably, both the ALG and ALG/CN-1% scaffolds demonstrated excellent biocompatibility, which was indicated by low hemolysis rates. In contrast, the Triton-X 100-treated group exhibited a higher rate of hemolysis. These results suggest that the fabricated hydrogel scaffolds are highly biocompatible and can be used as implantable biomaterials for *in vivo* bone regeneration studies.

2.8. *In vivo bone regeneration properties*

The promising physicochemical properties, excellent biocompatibility, and superior hemostatic ability of the 3D-printed ALG/CN hydrogel scaffolds motivated us to evaluate their potential for bone regeneration *in vivo*. Self-catalytic bone scaffolds have the advantage of augmenting bone healing with reduced inflammation and post-surgical infection risk [41–44,76,77]. Given its superior biocompatibility with hBMSCs and RAW 264.7 cells, we investigated the role of ALG/CN-1% hydrogel scaffold in bone regeneration. Pure ALG scaffold was used as the positive control, and the negative control group received no scaffold treatment. Fig. 7(a) provides a schematic overview of the *in vivo* study. After 5 weeks' post-implantation, the calvarial defect regions were excised and subjected to micro-CT, H&E, trichrome, and immunohistochemistry (IHC) staining analysis. Micro-CT analysis revealed bone regeneration ability of the scaffolds 5 weeks after surgery (Fig. 7(b)). The negative control (i.e., the control) group showed no noticeable bone formation, whereas the ALG-treated group (positive control) showed minimal new bone formation. Interestingly, the ALG/CN-1% group (experimental scaffold) showed significant new bone formation at 5 weeks' post-surgery. H&E staining further confirmed that the defects in
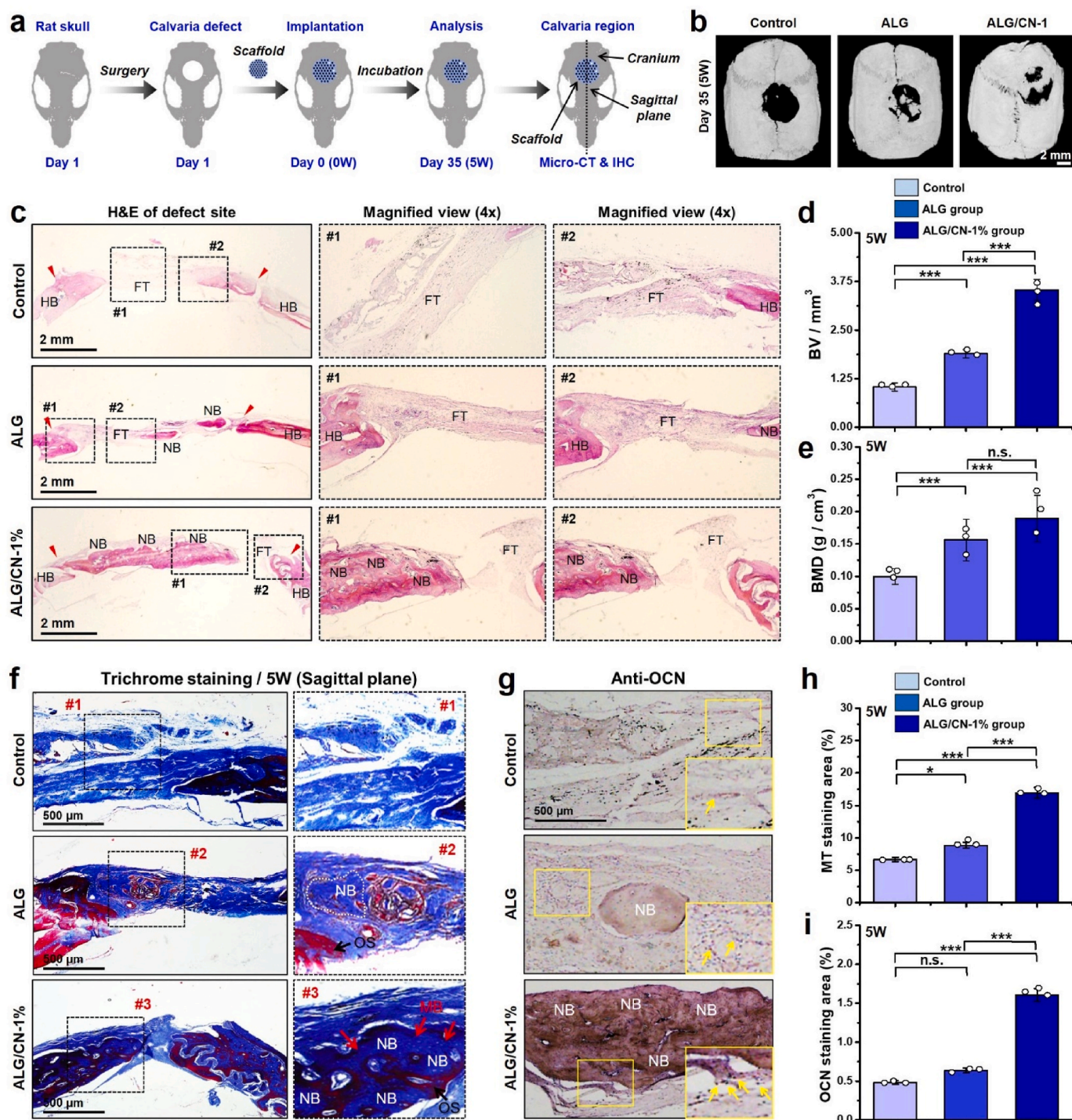
Fig. 7. *In vivo* bone regeneration study of the nanocomposite scaffolds after 5 weeks of implantation. **(a)** Schematics of the *in vivo* bone regeneration study. **(b)** Micro-CT images showing the new bone formation. Scale bar: 2 mm. **(c)** H&E staining images of the defect area showing the new bone formation. HB = host bone; NB = new bone; FT = fibrous tissue. Scale bar: 2 mm. **(d, e)** Quantitative analysis of the micro-CT analysis. **(f, h)** Trichrome staining images with corresponding quantification data. NB = new bone; MB (red color): mineralized/mature bone; OS = osteoid. Scale bar: 500 μm. **(g, i)** IHC staining of OCN protein markers in the new bone formation area with quantitative data. The yellow arrow indicates the OCN$^+$ cells. Scale bar: 500 μm. Data reported as mean ± s.d. of triplicated ($n = 3$) experiments, with statistical significance at *$p < 0.05$ and ***$p < 0.001$ (One-way ANOVA). (For interpretation of the references to color in this figure legend, the reader is referred to the Web version of this article.)

the control groups mainly comprised fibrous tissues (Fig. 7(c)). Moreover, the ALG-treated groups showed minimal new bone formation with 30–40 % fibrous tissue. However, the ALG/CN-1% group showed abundant newly formed bone in H&E with minimal fibrous tissue, suggesting its enhanced ability to regenerate new bone. The bone volume (BV) and bone mineral density (BMD) were significantly (***$p < 0.001$)

higher in the ALG/CN-1% groups than in the control and ALG-treated groups. To validate these findings, we further investigated collagen deposition in newly formed bone using trichrome staining. Fig. 7(f) revealed that collagen deposition in the calvaria cranial defect region was significantly higher in the ALG/CN-1% group than in other treatment groups, suggesting bone mineralization and bone matrix

14

remodeling. The relative trichrome staining area was significantly (***p < 0.001) larger in ALG/CN-1% groups than in control and ALG groups (Fig. 7(h)). Moreover, large amounts of osteoid (OS, immature bone; stained red) and fibrous tissue (FT) were found in both the control and ALG groups, indicating poor bone regeneration ability. Additionally, the ALG/CN-1% group exhibited more mineralized bone formation (MB; mature bone, stained deep blue) with thick collagen formation, suggesting enhanced osteogenesis and reduced osteoclastogenesis [78].

Immunostaining results further indicated that bone maturation was enhanced in the ALG/CN-1% group, as evidenced by the intense color of osteocalcin (OCN) expression in the defect region (Fig. 7(g)), which was not observed in the control and ALG groups. The OCN$^+$ staining area was significantly (***p < 0.001) larger in ALG/CN-1% (Fig. 7(i)), highlighting the potential of Ox-gCN-based oxygen-containing scaffolds in bone regeneration.

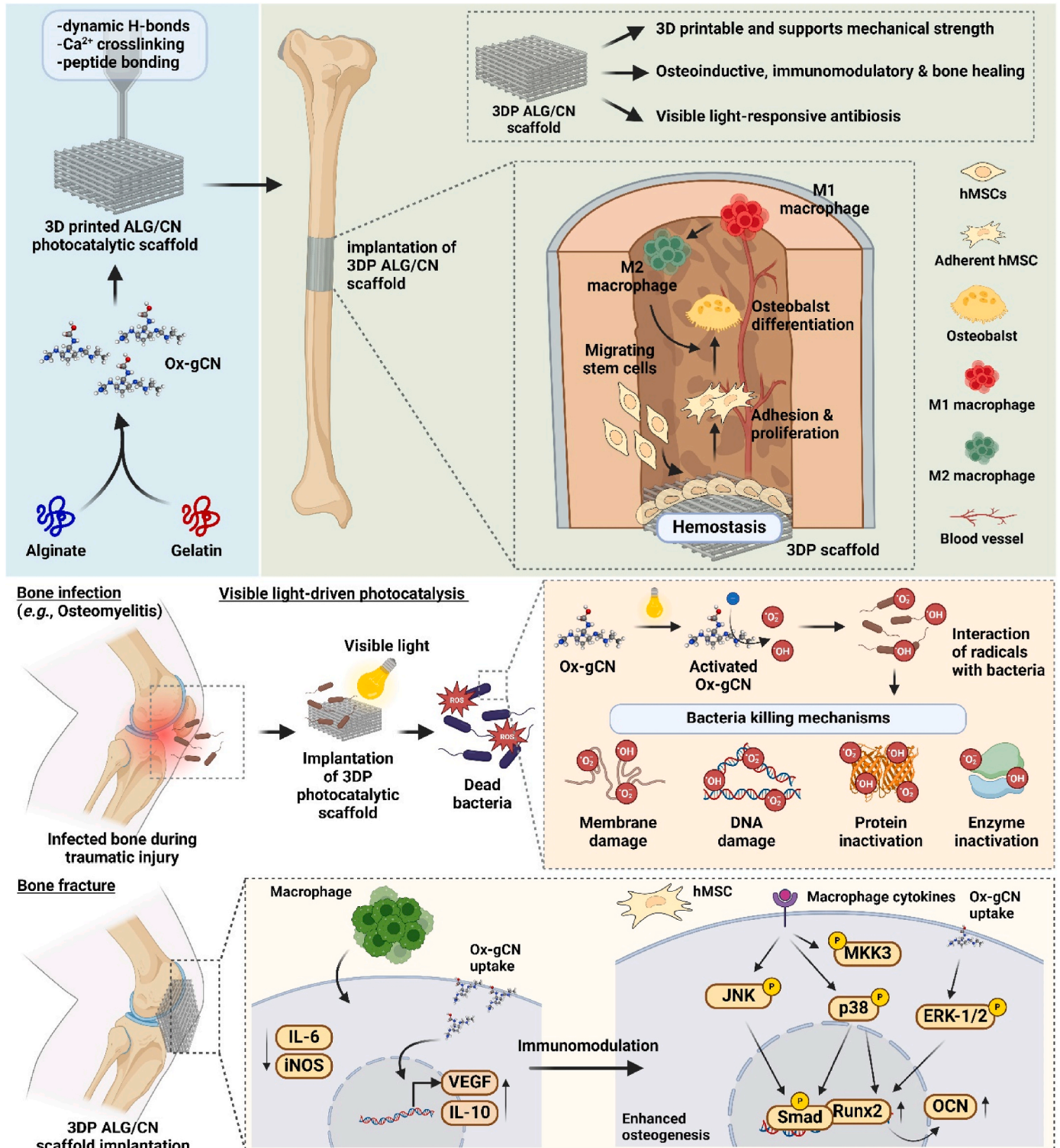During traumatic bone regeneration, the initial increase in pro-

Fig. 8. Schematic illustration of the mechanisms of the ALG/CN-based photocatalytic scaffold for enhanced antibacterial and osteoimmunomodulatory functions.

inflammatory cell activity at the fracture site transitions to a predominance of anti-inflammatory macrophages during the later phases of bone remodeling [79,80]. Therefore, immediate evaluation of the bone immune microenvironment is crucial for effective bone repair. The ICC staining results presented in Figs. S15(a and b) demonstrates higher expression of pro-inflammatory marker (iNOS) in the control group, which was significantly reduced (***$p < 0.001$) in the ALG and ALG/CN-1% groups, highlighting the tissue-healing potential of the fabricated photocatalytic scaffolds. Moreover, the expression of the anti-inflammatory marker (CD163) was significantly higher (***$p < 0.001$) in the ALG and ALG/CN-1% groups, indicating the activation of the anti-inflammatory osteoimmune microenvironment in the defect area after 5 weeks. The quantitative data for the percentage of CD163+ cells presented in Fig. S15(c) revealed a significant increase (***$p < 0.001$) in the ALG/CN-1% group than in other groups. The expression profiles of iNOS and CD163 were consistent with the *in vitro* qRT-PCR results, further supporting the effectiveness of the 3D-printed ALG/CN-1% photocatalytic scaffold in accelerating new bone formation through M2 macrophage polarization and simultaneous osteo-immunomodulation. Additionally, H&E-stained images of the major organs (kidney, liver, heart, lung, and spleen) 5 weeks after surgery (Fig. S16) revealed no noticeable morphological changes in the scaffold-treated group compared with the control group, suggesting that the fabricated ALG/CN-1% was highly biocompatible and clinically safe for *in vivo* applications. A schematic illustration of the mechanisms of the 3D-printed ALG/CN-based nano-photocatalytic scaffold for antibacterial and immunomodulatory bone regeneration is shown in Fig. 8.

3. Conclusion

Our study demonstrated the application of 3D printable hydrogel inks reinforced with oxygen-doped 2D carbon nitrides with biomimetic properties for multifunctional bone regeneration *in vitro* and *in vivo*. The fabricated nano/biocomposite scaffolds were bioactive and non-toxic to hBMSCs and RAW 264.7 cells, providing a desirable adhesion, proliferation, and differentiation platform. Interestingly, the visible light-responsiveness and self-catalytic properties of the 3D-printed ALG/CN scaffold were used for investigating the biofilm reduction efficacy against gram-negative (*E. coli*) and positive (*S. epidermidis*) bacteria through the generation of • O_2 and • OH radicals. Moreover, the oxygen-rich 3D-printed ALG/CN-1% scaffold enhanced hBMSCs proliferation, migration, mineralized nodule formation, and osteogenesis by upregulating the osteoblast-specific transcription factors (*Runx2, ALP, OCN, OPN,* and *COL1A*) *in vitro*. Furthermore, the scaffolds displayed superior M2 macrophage polarization potential through phosphorylation of ERK (p-ERK-1/2), MAPK (p-MKK3 and p38), and p-JNK signaling proteins and induced the activation of anti-inflammatory genes (*Arg-1, TGF-β,* and *VEGF*). Notably, the ALG/CN-1% scaffolds demonstrated exceptional potential for bone regeneration in a rat calvaria defect model, characterized by reduced inflammation and excellent biocompatibility, as confirmed by H&E staining, trichrome staining, micro-CT, ICC, and IHC analysis. In summary, we fabricated a self-catalytic oxygen-rich 3D printed scaffold with desirable osteo-immunomodulatory and hemostatic properties offering promising potential for ameliorating traumatic bone injury in clinical settings.

4. Experimental section

4.1. Materials

Sodium alginate from brown algae (Alg; purity >99 %), gelatin from porcine skin (Gel; type A, gel strength ~300 g bloom), melamine (purity >99 %), urea (purity >99 %), and calcium chloride (anhydrous, purity >97 %) were purchased from Sigma-Aldrich, USA. Sulfuric acid (H_2SO_4, purity 98 %) and hydrogen peroxide (H_2O_2, 35 % *v/v*) were obtained from Daejung Chemicals, Republic of Korea. Dulbecco's modified Eagles

media (DMEM) and phosphate buffer saline (PBS) were obtained from Welgene, Republic of Korea. Fetal bovine serum (FBS) and Anti-Anti (penicillin-streptomycin antibiotics) were purchased from Gibco-BRL, USA. All the chemicals were used as-received unless stated elsewhere.

4.2. Synthesis of g-C_3N_4 and Ox-gC_3N_4

In a typical synthesis procedure, 10 g Melamine and 10 g Urea were mixed and ground well in an agate mortar for 15 min. Subsequently, the mixture was placed in a crucible with a cover and thermally treated at 550 °C for 3 h in a muffle furnace with a ramping rate of 10 °C/min. After natural cooling, the sample was collected and ground into powder. Urea and melamine undergo thermal decomposition and polycondensation, resulting in 2D-structured g-C_3N_4 (g-CN) nanosheets. The oxidized g-CN (Ox-gCN) was synthesized according to a previous report [46], keeping the oxidation time of 60 min to cultivate ultrasmall Ox-gCN flakes.

4.3. Fabrication of ALG/CN hydrogel inks

The hydrogel was fabricated using a ratio of Alg and Gel, as reported in our previous study, owing to its superior printability [6]. Briefly, 3 % (*w/v*) Alg was dissolved in sterile deionized water by stirring at 65 °C. After that, the temperature of the solution was brought to 45 °C, and the Gel (4 % *w/v*) was slowly added to the mixture until a homogenized solution was obtained. Next, various concentrations of Ox-CN (0, 0.5, 1, 2, and 4 *wt*%) were added with respect to the weight of the Alg/Gel and stirred overnight at 45 °C. After that, the hydrogel pre-solution was bath sonicated to remove the excess bubbles, followed by storage at 4 °C until further use. This allowed the physical crosslinking between Alg, Gel, and Ox-gCN. The nanocomposite hydrogels were designated as ALG/CN$_x$ %, where '*x*' is the *wt*.% of Ox-gCN, respectively.

4.4. 3D printing of nanocomposite hydrogels

The 3D printing was carried out using a commercial 3D bioprinter (Cellink Bio-X, Sweden) equipped with a temperature-controlled print head and bed (range ~4–60 °C). Before 3D printing, the nanocomposite hydrogel inks were thawed at 37 °C and loaded onto the printing cartridge (3 mL/cartridge, Cellink, Sweden). After that, the hydrogel inks were chilled at 4 °C for 30 min. The 3D printing was carried out using a 4 °C print bed, keeping the print head at 10 °C with a print speed and extrusion pressure of 4 mm/s and 120 kPa, respectively. The print geometry ($20 \times 20 \times 5$ mm^3) was designed using SolidWorks software (Dassault Biosystems, France). After 3D printing, each construct was crosslinked with a 100 mM CaCl$_2$ solution for 10–15 min. After chemical crosslinking, the hydrogels were washed with 1 × PBS and stored at 4 °C until future use.

4.5. Characterizations

4.5.1. General characterizations

The bulk g-CN and Ox-gCN morphology were evaluated using a field emission scanning electron microscope (FE-SEM; JSM-7900F, Jeol, Japan) in a gentle beam (GB) mode with a 5 kV/cm operating voltage. The intrinsic structure of the g-CN and Ox-gCN was observed using a transmission electron microscope (TEM; JEM-2100F, Jeol, Japan). The structural and functional property of the g-CN and Ox-gCN was investigated using the X-ray diffractometer (XRD; X'Pert Pro MPD, PANalytical, Netherlands; Al-kα, $hv = 1486.6$ eV) and Fourier transform infrared (FT-IR; iN10/iS50, Thermo Scientific, USA) spectroscopy. The surface functional groups and the elemental states of the synthesized g-CN and Ox-gCN were evaluated by X-ray photoelectron spectroscopy (XPS; K Alpha+, Thermo VG, Thermo Scientific, UK). A photoluminescence (PL) spectrometer (Quanta Master, Photon Technology International, USA) and Horiba (Nanolog, equipped with 450 W Xe lamp

and a CCD detector with N_2 cooler) were used to measure the PL spectra of the g-CN and Ox-gCN. The UV–visible spectra of the samples were recorded using a UV–Vis spectrophotometer (Varian Cary 100, Spectralab Scientific, USA).

4.5.2. Hydrogel characterizations

The 3D printed and freeze-dried hydrogel scaffold morphology was investigated using an FE-SEM with an operating voltage of 15 kV/cm under lower electron detector (LED) mode and a probe current of 500 nA. The chemical interaction of the hydrogel components was analyzed using an FT-IR spectrophotometer (iN10/iS50, Thermo Scientific, USA). The viscoelastic property of the hydrogel inks was investigated using a rotational rheometer (Anton Parr, Germany) with a 20 mm parallel plate. The hydrogels were characterized by oscillatory strain sweep (0.1–1000 %, 1 Rad/s), frequency sweep (0.1–100 Rad/s, 1 % strain), and thixotropic (0.1/s-1000/s-0.1/s shear rate, 300 s) tests at room temperature (25 °C). The shear thinning property of the hydrogel inks was evaluated through a viscosity vs. shear rate (0.1–100/s) study at 10 °C. The swelling efficiency and degradation study were performed as reported in our previous study [6]. The experimental details are given in the Supporting **Methods** section.

4.6. In vitro cytocompatibility tests

4.6.1. Cell viability assays

The human bone marrow-derived mesenchymal stem cells (hBMSCs) were obtained from the College of Dentistry, Seoul National University, Republic of Korea. The murine monocyte (RAW 264.7) cells were received from the Korean Cell Line Bank (KCLB), Seoul National University, Republic of Korea. The cells were maintained in DMEM media supplemented with 10 % FBS and 1 % antibiotics in a humidified atmosphere with 5 % CO_2 at 37 °C. The cell viability of the hBMSCs and RAW 264.7 cells in the presence of 3D printed hydrogel was assessed using the water-soluble tetrazolium test (WST-8) and live/dead staining assay at different time points. Details of the cell viability test are given in our previous study. For the cell viability and in vitro osteogenic differentiation study, passage-3 of hBMSCs was used unless stated elsewhere.

4.6.2. In vitro osteogenic differentiation study

The in vitro osteogenic differentiation potential of hBMSCs in the presence of fabricated scaffolds was evaluated using alizarin Red-S (ARS) staining, alkaline phosphatase (ALP) assay, immunocytochemical (ICC) staining, and quantitative real-time PCR (qRT-PCR) assays after 7 and 14 days of incubation. The hBMSCs were cultured in a scaffold leaching medium containing the osteogenic differentiation factors and incubated for desired time points. A detailed protocol for in vitro osteogenic differentiation study is given in the Supporting **Methods** section.

4.6.3. In vitro macrophage polarization and osteoimmunomodulation study

The in vitro macrophage polarization potential of the fabricated scaffolds was evaluated using RAW 264.7 cells. The polarization study assessed the morphology, expression of inflammatory gene markers and immunocytochemical (ICC) assays. Lipopolysaccharide (LPS, 200 ng/mL) was used as a positive control for all experiments. Plates without any treatment were considered the negative control. The detailed experimental protocol for RAW 264.7 cell polarization is given in the Supporting **Methods** section.

4.7. Photocatalytic performance of the scaffolds

Rhodamine B (RhB) dye was chosen as the model compound to test the photo-degradation efficiency of the ALG/CN-1% scaffold (photocatalyst) under visible light irradiation. All the photo-degradation experiments were carried out at ambient temperature using 20 mg of photocatalyst in 100 mL of RhB (4 ppm). During the photo-degradation

experiments, the source of visible light was a solar simulator 100 W Xe lamp. The reaction temperature was maintained constant using a water circulation regulator. The catalyst was homogeneously dispersed by stirring at 250 rpm. To ensure the attainment of adsorption-desorption equilibrium between the photocatalyst and the dye mixture, the solution was kept in the dark while stirring for 30 min before illumination with light. 4.0 mL of the sample solution was pipetted and centrifuged after certain intervals. Ultraviolet–visible (UV–Vis) absorption spectra of the photo-degraded sample were recorded at 554 nm to monitor the concentration during the photoreaction.

4.8. In vitro visible-light-induced antibacterial properties

The in vitro antibacterial property of the fabricated hydrogel scaffolds was evaluated under visible light owing to the presence of photo-responsive g-C_3N_4 (g-CN). The antibacterial test was conducted using a gram-negative (Escherichia coli, ATCC) and a gram-positive bacterium (Staphylococcus epidermidis, ATCC) as a model through agar plate assay, live/dead staining (SYTO9/PI), biofilm reduction test (crystal violet staining), and SEM analysis.

The bacterial stock was grown overnight in the nutrient broth (Difco™, BD Biosciences, USA) media at 37 °C under gentle stirring (120 rpm). The bacteria viability was confirmed by measuring the absorbance at 600 nm (OD_{600} = 0.423) as a function of peptidoglycan and ions. For the agar plate assay, 5 mL of each bacteria solution (final concentration = 1×10^{-5}/mL) was incubated with ~100 mg (one printed scaffold) of samples in a 100 mL Erlenmeyer flask for 2–4 h at 37 °C. After that, the flasks were randomly divided into (1) w/o light irradiation group and (2) w/light irradiation group, respectively. The bacteria + scaffold samples were taken in a reaction pot (100 mL) and illuminated under visible light (Xe lamp, Power: 100 W) under constant stirring (50 rpm) for 10 min for the light-irradiated group. After the light treatment, the samples were additionally incubated for 12 h at 37 °C. Next, each group's 100 μL of bacteria suspension was taken in fresh conical tubes and diluted to achieve a final concentration of 10^{-5}. The diluted bacteria sample (50 μL) was spread over the nutrient agar plates and further incubated for 12 h at 37 °C. The colony formation was photographed, and the bacterial coverage was quantified using ImageJ software (v1.8, NIH, Bethesda, USA).

For live/dead assay, the bacteria suspension was incubated with 5 μL of SYTO9/PI (Thermo-Fischer Scientific, USA) staining solution for 10–20 min at 37 °C. After that, the bacteria samples were imaged using a confocal laser scanning microscope (LSM-880, Carl Zeiss, Germany) with an $^{ex}/_{em}$ of $^{488}/_{503}$ nm and $^{535}/_{617}$ nm, respectively. The images were acquired using ZEN v2017 (Zeiss, Germany) software and merged in ImageJ (v1.8, NIH, Bethesda, USA). For the anti-biofilm test, the bacteria samples were incubated with hydrogels for 24 h, followed by light irradiation for 10 min. After that, the hydrogel residues were carefully removed from the well plates, and the biofilm was stained with 500 μL of crystal violet (0.4 % w/v in methanol) for 15 min at room temperature. After that, the excess stain was washed with $1 \times$ PBS, and the plates were air dried. The biofilm formation was photographed, and the staining area (%) was calculated using ImageJ software (v1.8, NIH, Bethesda, USA). FE-SEM was conducted to study the morphology of bacteria. For SEM analysis, the bacteria suspension was centrifuged at 10,000 rpm, followed by fixation with 2 % glutaraldehyde/para-formaldehyde (Sigma-Aldrich, USA), gradient dehydration with ethanol, and finally washed with HDMS solution. The SEM images were acquired at 5 kV/cm under gentle beam (GB) mode with a current density of 100 nA.

4.9. In vitro hemostatic performance

4.9.1. Clotting time study

The in vitro hemostatic performance of the fabricated hydrogel scaffolds was investigated through clotting time assay according to a

protocol reported previously. Fresh blood from mice was collected and mixed with sodium citrate buffer in an Eppendorf tube. After that, 20 μL of 100 mM $CaCl_2$ was mixed with the citrated blood and vortexed for 10 s. Next, 50 μL of the blood sample was carefully injected into the 96-well plates containing the hydrogel samples (10 mg). We used an ALG/CN-1% hydrogel sample based on the outstanding *in vitro* results. The pure ALG hydrogel and commercial gauge were taken as positive controls. After different time points, 100 μL of PBS was added to each well to stop the clotting, and the supernatant was collected in another well. The clotting time was marked in each well by observing the uniform clot formation. To investigate the microscopic clot formation, we further performed the FE-SEM analysis. For this, the hydrogel samples were fixed in 2 % glutaraldehyde/paraformaldehyde (1:1 ratio) for 12 h, followed by gradient-dehydration with ethanol, final wash with hexamethyldisilazane (HDMS), and then visualized by the SEM instrument. The operating voltage for the SEM analysis was 15 kV/cm under lower electron detector (LED) mode and a probe current of 500 nA.

4.9.2. Analysis of blood clotting index (BCI)

Initially, 50 mg of the newly created scaffold was placed onto glass plates and left to incubate at 37 °C for 10 min. Subsequently, 200 μL of fresh blood containing an anticoagulant was introduced and incubated for 5 min. Finally, 15 mL of deionized water was carefully added to the plates. The surgical gauge is used as technical control in commercial settings. A reference control was prepared by combining 200 μL of pure blood sample with 15 mL of deionized water. The specimens were positioned on the shaker and subjected to a rotational speed of 30 revolutions per minute for 10 min. The absorbance was quantified using a microplate reader at a wavelength of 540 nm, and the Blood Clotting Index (BCI) was calculated using the following equation:

$$BCI\ (\%) = \frac{O.D._{sample}}{O.D._{Reference\ control}} \times 100\%$$

4.9.3. Study of red blood cells (RBCs) attachment

To investigate the adhesion of red blood cells (RBCs), 50 mg of the hydrogel scaffold that was created was placed into glass test tubes. Subsequently, 200 μL of RBC suspension was introduced and incubated for 1 h at 37 °C. Following a 1-h incubation period to eliminate unbound RBCs, the samples underwent three rounds of washing with normal saline. After washing, 5 mL of deionized water was introduced to the superabsorbent material with attached RBCs. The mixture was then incubated for 1 h to induce hemolysis of the attached RBCs. The positive control consisted of 5 mL of deionized water and 200 μL of RBC suspension. Next, a sample of the liquid above the sediment was taken, and the amount of light absorbed at a wavelength of 540 nm was measured using a microplate reader device. The percentage of connected red blood cells (RBCs) was calculated using the following equation:

$$\%\ of\ RBCs\ attachment = \frac{O.D._{sample}}{O.D._{control}} \times 100\%$$

4.9.4. Hemolysis study

The hemocompatibility of the fabricated hydrogels was evaluated by monitoring the hemolysis test as reported elsewhere. Briefly, fresh blood from 2 to 3 weeks-old mice was collected in an Eppendorf tube. The red blood cells (RBCs) were then collected by centrifuging the whole blood at 1000 rpm for 10 min at 20–25 °C. Next, the RBCs were collected by washing them thrice in 1 × PBS. A final concentration of 10 % (*v/v*) RBCs was used for the hemolysis study. For the assay, 10 mg of ALG and ALG/CN-1% hydrogel was taken in a 24-well plate and incubated with 1 mL of 10 % (*v/v*) RBCs for 120 min at 37 °C under gentle shaking (100 rpm). After 120 min, the RBCs were collected into fresh Eppendorf tubes and centrifuged at 1000 rpm for 10 min at 20–25 °C. Next, 100 μL of the supernatant was taken into a 96-well plate, and the absorbance of free hemoglobin (Hb) was quantified by measuring the absorbance at 540

nm using a microplate reader (Infinite® M Nano 200 Pro, TECAN, Switzerland). Plates with PBS and Triton-X 100 (0.1 % *v/v*) were considered negative and positive controls. The hemolysis percentage (%) was calculated according to the following equation:

$$\%\ hemolysis = \frac{(Ab_S - Ab_{NEG})}{(Ab_{POS} - Ab_{NEG})} \times 100$$

where Ab_S, Ab_{POS}, and Ab_{NEG} are the absorbance of the sample, positive control, and negative control, respectively.

4.10. In vivo bone regeneration study

Based on the outstanding *in vitro* results, we selected the 3D printed ALG/CN-1% scaffold for studying the *in vivo* bone regeneration using a rat calvaria critical defect model after 5 weeks of treatment. The defects without any scaffold and ALG scaffold were taken as the negative and positive control, respectively. After 5 weeks post-implantation, the *in vivo* bone regeneration potential was studied by micro-CT (μCT), hematoxylin and eosin (H&E) staining, and Masson's Trichrome (MT) staining to evaluate the endogenous bone formation and collagen deposition. The immunohistochemical (IHC) analysis was performed to evaluate the expression of OCN expression in the newly formed bone region. Details of the animal surgery, scaffold implantation, and staining procedures are given in the Supporting **Methods** section.

4.11. Statistical analysis

The statistical analysis was performed using Origin Pro v9.0 software (Origin Labs, USA). Data reported as mean ± s.d. of triplicate ($n = 3$) experiments. The significant difference between the control and treatment groups was evaluated using the One-way Analysis of Variance (ANOVA) test. The statistical significance was considered at $*p < 0.05$, $**p < 0.01$, and $***p < 0.001$. A value above this level was considered not significant (n.s.). For cytochemical assays, at least five ($n = 5$) independent images were assessed using ImageJ software, and the significance level was analyzed with a *p*-value <0.05.

CRediT authorship contribution statement

Sayan Deb Dutta: Writing – review & editing, Writing – original draft, Visualization, Software, Methodology, Investigation, Formal analysis, Data curation, Conceptualization. **Jin Hexiu:** Methodology, Data curation. **Md Moniruzzaman:** Writing – review & editing, Software, Resources, Methodology, Data curation. **Tejal V. Patil:** Writing – review & editing, Validation, Methodology. **Rumi Acharya:** Validation, Software, Methodology. **Jong Sung Kim:** Supervision, Investigation, Funding acquisition. **Ki-Taek Lim:** Writing – review & editing, Supervision, Project administration, Investigation, Funding acquisition.

Declaration of competing interest

The authors declare that they have no known competing financial interests or personal relationships that could have appeared to influence the work reported in this paper.

Acknowledgments

Research Program' also supported this research through the 'National Research Foundation of Korea' (NRF), funded by the Ministry of Education (NRF–2021R1A6A1A03038996 and 2022R1G1A1010780).

Appendix A. Supplementary data

Supplementary data to this article can be found online at https://doi.org/10.1016/j.biomaterials.2024.122991.

Data availability

Data will be made available on request.

References

[1] L. Wu, X. Pei, B. Zhang, Z. Su, X. Gui, C. Gao, L. Guo, H. Fan, Q. Jiang, L. Zhao, 3D-printed HAp bone regeneration scaffolds enable nano-scale manipulation of cellular mechanotransduction signals, Chem. Eng. J. 455 (2023) 140699.

[2] A.L. Farris, D. Lambrechts, Y. Zhou, N.Y. Zhang, N. Sarkar, M.C. Moorer, A. N. Rindone, E.L. Nyberg, A. Perdomo-Pantoja, S. Burris, 3D-printed oxygen-releasing scaffolds improve bone regeneration in mice, Biomaterials 280 (2022) 121318.

[3] M. Zhang, X. Zhai, T. Ma, Y. Huang, M. Jin, H. Yang, H. Fu, S. Zhang, T. Sun, X. Jin, Sequential therapy for bone regeneration by cerium oxide-reinforced 3D-printed bioactive glass scaffolds, ACS Nano 17 (5) (2023) 4433–4444.

[4] S.D. Dutta, K. Ganguly, A. Randhawa, T. Patil, D.K. Patel, K.-T. Lim, Electrically stimulated 3D bioprinting of gelatin-polypyrrole hydrogel with dynamic semi-IPN network induces osteogenesis via collective signaling and immunopolarization, Biomaterials (2023) 121999.

[5] S.D. Dutta, K. Ganguly, T.V. Patil, A. Randhawa, K.-T. Lim, Unraveling the potential of 3D bioprinted immunomodulatory materials for regulating macrophage polarization: state-of-the-art in bone and associated tissue regeneration, Bioact. Mater. 28 (2023) 284–310.

[6] S.D. Dutta, J. Hexiu, D.K. Patel, K. Ganguly, K.-T. Lim, 3D-printed bioactive and biodegradable hydrogel scaffolds of alginate/gelatin/cellulose nanocrystals for tissue engineering, Int. J. Biol. Macromol. 167 (2021) 644–658.

[7] M.A. Skylar-Scott, J. Mueller, C.W. Visser, J.A. Lewis, Voxelated soft matter via multimaterial multinozzle 3D printing, Nature 575 (7782) (2019) 330–335.

[8] V. Mironov, T. Boland, T. Trusk, G. Forgacs, R.R. Markwald, Organ printing: computer-aided jet-based 3D tissue engineering, Trends Biotechnol. 21 (4) (2003) 157–161.

[9] S.V. Murphy, A. Atala, 3D bioprinting of tissues and organs, Nat. Biotechnol. 32 (8) (2014) 773–785.

[10] L.Y. Zhou, J. Fu, Y. He, A review of 3D printing technologies for soft polymer materials, Adv. Funct. Mater. 30 (28) (2020) 2000187.

[11] I.R. Avanzi, J.R. Parisi, A. Souza, M.A. Cruz, C.C.S. Martignago, D.A. Ribeiro, A.R. C. Braga, A.C. Renno, 3D-printed hydroxyapatite scaffolds for bone tissue engineering: a systematic review in experimental animal studies, J. Biomed. Mater. Res. B Appl. Biomater. 111 (1) (2023) 203–219.

[12] Z. Xu, X. Qi, M. Bao, T. Zhou, J. Shi, Z. Xu, M. Zhou, A.R. Boccaccini, K. Zheng, X. Jiang, Biomineralization inspired 3D printed bioactive glass nanocomposite scaffolds orchestrate diabetic bone regeneration by remodeling micromilieu, Bioact. Mater. 25 (2023) 239–255.

[13] L. Yang, L. Fan, X. Lin, Y. Yu, Y. Zhao, Pearl powder hybrid bioactive scaffolds from microfluidic 3D printing for bone regeneration, Adv. Sci. 10 (34) (2023) 2304190.

[14] X. Mi, Z. Su, Y. Fu, S. Li, A. Mo, 3D printing of Ti3C2-MXene-incorporated composite scaffolds for accelerated bone regeneration, Biomed. Mater. 17 (3) (2022) 035002.

[15] L. Liu, J. Wu, S. Lv, D. Xu, S. Li, W. Hou, C. Wang, D. Yu, Synergistic effect of hierarchical topographic structure on 3D-printed Titanium scaffold for enhanced coupling of osteogenesis and angiogenesis, Materials Today Bio 23 (2023) 100866.

[16] J. Chen, H. Zhou, Y. Fan, G. Gao, Y. Ying, J. Li, 3D printing for bone repair: coupling infection therapy and defect regeneration, Chem. Eng. J. (2023) 144537.

[17] Q. Li, H. Yu, F. Zhao, C. Cao, T. Wu, Y. Fan, Y. Ao, X. Hu, 3D printing of microenvironment-specific bioinspired and exosome-reinforced hydrogel scaffolds for efficient cartilage and subchondral bone regeneration, Adv. Sci. 10 (26) (2023) 2303650.

[18] X. Hu, Z. Zhang, H. Wu, S. Yang, W. Zhao, L. Che, Y. Wang, J. Cao, K. Li, Z. Qian, Progress in the application of 3D-printed sodium alginate-based hydrogel scaffolds in bone tissue repair, Biomater. Adv. (2023) 213501.

[19] D.K. Patel, S.D. Dutta, J. Hexiu, K. Ganguly, K.-T. Lim, 3D-printable chitosan/silk fibroin/cellulose nanoparticle scaffolds for bone regeneration via M2 macrophage polarization, Carbohydr. Polym. 281 (2022) 119077.

[20] J. Liu, L. Sun, W. Xu, Q. Wang, S. Yu, J. Sun, Current advances and future perspectives of 3D printing natural-derived biopolymers, Carbohydr. Polym. 207 (2019) 297–316.

[21] G. Basara, M. Saeidi-Javash, X. Ren, G. Bahcecioglu, B.C. Wyatt, B. Anasori, Y. Zhang, P. Zorlutuna, Electrically conductive 3D printed Ti3C2Tx MXene-PEG composite constructs for cardiac tissue engineering, Acta Biomater. 139 (2022) 179–189.

[22] M. Najarzadegan, S.N. Khorasani, S. Khalili, M.R. Molavian, S. Saleki, A. Kakapour, M. Hafezi, A new shear-thinning nanocomposite hydrogel from GelMA-GO for soft tissue engineering, Eur. Polym. J. (2023) 112204.

[23] C.S. Cabral, S.P. Miguel, D. de Melo-Diogo, R.O. Louro, I.J. Correia, Green reduced graphene oxide functionalized 3D printed scaffolds for bone tissue regeneration, Carbon 146 (2019) 513–523.

[24] J. Zhang, H. Eyisoylu, X.-H. Qin, M. Rubert, R. Müller, 3D bioprinting of graphene oxide-incorporated cell-laden bone mimicking scaffolds for promoting scaffold fidelity, osteogenic differentiation and mineralization, Acta Biomater. 121 (2021) 637–652.

[25] Q. Yang, H. Yin, T. Xu, D. Zhu, J. Yin, Y. Chen, X. Yu, J. Gao, C. Zhang, Y. Chen, Engineering 2D mesoporous Silica@ MXene-integrated 3D-printing scaffolds for combinatory osteosarcoma therapy and NO-augmented bone regeneration, Small 16 (14) (2020) 1906814.

[26] J. Zhang, H. Chen, M. Zhao, G. Liu, J. Wu, 2D nanomaterials for tissue engineering application, Nano Res. 13 (2020) 2019–2034.

[27] Y. Zheng, X. Hong, J. Wang, L. Feng, T. Fan, R. Guo, H. Zhang, 2D nanomaterials for tissue engineering and regenerative nanomedicines: recent advances and future challenges, Adv. Healthcare Mater. 10 (7) (2021) 2001743.

[28] A. Halim, K.-Y. Qu, X.-F. Zhang, N.-P. Huang, Recent advances in the application of two-dimensional nanomaterials for neural tissue engineering and regeneration, ACS Biomater. Sci. Eng. 7 (8) (2021) 3503–3529.

[29] B. Li, H. Zhu, Y. Lv, C. Wang, S. Wu, S. Zhu, Y. Zheng, H. Jiang, Y. Zhang, Z. Li, Metal ion coordination improves graphite nitride carbon microwave therapy in antibacterial and osteomyelitis treatment, Small 19 (47) (2023) 2303484.

[30] B. Fan, L. Xing, Q. He, F. Zhou, X. Yang, T. Wu, G. Tong, D. Wang, W. Wu, Selective synthesis and defects steering superior microwave absorption capabilities of hollow graphitic carbon nitride micro-polyhedrons, Chem. Eng. J. 435 (2022) 135086.

[31] N.S. Heo, H.P. Song, S.M. Lee, H.-J. Cho, H.J. Kim, Y.S. Huh, M.I. Kim, Rosette-shaped graphitic carbon nitride acts as a peroxidase mimic in a wide pH range for fluorescence-based determination of glucose with glucose oxidase, Microchim. Acta 187 (2020) 1–11.

[32] P. Mane, H. Bae, V. Burungale, S.-W. Lee, M. Misra, H. Parbat, A.N. Kadam, J.-S. Ha, Interface-engineered Z-scheme of BiVO4/g-C3N4 photoanode for boosted photoelectrochemical water splitting and organic contaminant elimination under solar light, Chemosphere 308 (2022) 136166.

[33] A.N. Kadam, H. Kim, S.-W. Lee, Low-temperature in situ fabrication of porous S-doped g-C3N4 nanosheets using gaseous-bubble template for enhanced visible-light photocatalysis, Ceram. Int. 46 (18) (2020) 28481–28489.

[34] Z. Teng, N. Yang, H. Lv, S. Wang, M. Hu, C. Wang, D. Wang, G. Wang, Edge-functionalized g-C3N4 nanosheets as a highly efficient metal-free photocatalyst for safe drinking water, Chem 5 (3) (2019) 664–680.

[35] S. Demirci, S.S. Suner, O.U. Neli, A. Koca, N.B.P. Sahiner, S heteroatom doped, bio- and hemo-compatible 2D graphitic-carbon nitride (g-C3N4) with antioxidant, light-induced antibacterial, and bioimaging endeavors, Nanotechnology 35 (2) (2023) 025101.

[36] J.N. Tiwari, Y.-K. Seo, T. Yoon, W.G. Lee, W.J. Cho, M. Yousuf, A.M. Harzandi, D.-S. Kang, K.-Y. Kim, P.-G. Suh, Accelerated bone regeneration by two-photon photoactivated carbon nitride nanosheets, ACS Nano 11 (1) (2017) 742–751.

[37] M. Davardoostmanesh, H. Ahmadzadeh, E.K. Goharshadi, A. Meshkini, E. Sistanipour, Graphitic carbon nitride nanosheets prepared by electrophoretic size fractionation as an anticancer agent against human bone carcinoma, Mater. Sci. Eng. C 111 (2020) 110803.

[38] U.V. Priya, A. Saranya, P.V. Prasath, K. Ravichandran, Investigation of in vitro biological studies on Fe doped hydroxyapatite-graphitic carbon nitride composite, Mater. Today: Proc. 68 (2022) 43–49.

[39] C. Gao, P. Feng, S. Peng, C. Shuai, Carbon nanotube, graphene and boron nitride nanotube reinforced bioactive ceramics for bone repair, Acta Biomater. 61 (2017) 1–20.

[40] B. Danagody, N. Bose, K. Rajappan, A. Iqbal, G.M. Ramanujam, A.K. Anilkumar, Electrospun PAN/PEG nanofibrous membrane embedded with a MgO/gC3N4 nanocomposite for effective bone regeneration, ACS Biomater. Sci. Eng. 10 (1) (2023) 468–481.

[41] L. Liu, Z. Zhang, M. Aimaijiang, M. Liu, L. Huang, Z. Pan, S. Liu, S. Qi, X. Zhang, H. Wang, Strontium-incorporated carbon nitride nanosheets modulate intracellular tension for reinforced bone regeneration, Nano Lett. 22 (23) (2022) 9723–9731.

[42] A.A. Sadek, M. Abd-Elkareem, H.N. Abdelhamid, S. Moustafa, K. Hussein, Repair of critical-sized bone defects in rabbit femurs using graphitic carbon nitride (g-C3N4) and graphene oxide (GO) nanomaterials, Sci. Rep. 13 (1) (2023) 5404.

[43] G.P. Awasthi, V.K. Kaliannagounder, J. Park, B. Maharjan, M. Shin, C. Yu, C. H. Park, C.S. Kim, Assembly of porous graphitic carbon nitride nanosheets into electrospun polycaprolactone nanofibers for bone tissue engineering, Colloids Surf. A Physicochem. Eng. Asp. 622 (2021) 126584.

[44] A. Papaioannou, E. Vasilaki, K. Loukelis, D. Papadogianni, M. Chatzinikolaidou, M. Vamvakaki, Bioactive and biomimetic 3D scaffolds for bone tissue engineering using graphitic carbon nitride as a sustainable visible light photoinitiator, Biomater. Adv. 157 (2024) 213737.

[45] Y. Zhou, Y. Wu, H. Wu, J. Xue, L. Ding, R. Wang, H. Wang, Fast hydrogen purification through graphitic carbon nitride nanosheet membranes, Nat. Commun. 13 (1) (2022) 5852.

[46] Z. Teng, H. Lv, C. Wang, H. Xue, H. Pang, G. Wang, Bandgap engineering of ultrathin graphene-like carbon nitride nanosheets with controllable oxygenous functionalization, Carbon 113 (2017) 63–75.

[47] Y. Yang, Z. Bian, Oxygen doping through oxidation causes the main active substance in g-C3N4 photocatalysis to change from holes to singlet oxygen, Sci. Total Environ. 753 (2021) 141908.

[48] P. Niu, L. Zhang, G. Liu, H.M. Cheng, Graphene-like carbon nitride nanosheets for improved photocatalytic activities, Adv. Funct. Mater. 22 (22) (2012) 4763–4770.

[49] A. Dunaev, I. Arkhangelsky, Y.V. Zubavichus, V. Avdeev, Preparation, structure and reduction of graphite intercalation compounds with hexachloroplatinic acid, Carbon 46 (5) (2008) 788–795.

[50] H.-J. Li, B.-W. Sun, L. Sui, D.-J. Qian, M. Chen, Preparation of water-dispersible porous gC 3 N 4 with improved photocatalytic activity by chemical oxidation, Phys. Chem. Chem. Phys. 17 (5) (2015) 3309–3315.

[51] K. Rosińska, M. Bartniak, A. Wierzbicka, A. Sobczyk-Guzenda, D. Bociaga, Solvent types used for the preparation of hydrogels determine their mechanical properties and influence cell viability through gelatine and calcium ions release, J. Biomed. Mater. Res. B Appl. Biomater. 111 (2) (2023) 314–330.

[52] D.K. Patel, K. Ganguly, J. Hexiu, S.D. Dutta, T.V. Patil, K.-T. Lim, Functionalized chitosan/spherical nanocellulose-based hydrogel with superior antibacterial efficiency for wound healing, Carbohydr. Polym. 284 (2022) 119202.

[53] I. Francolini, E. Perugini, I. Silvestro, M. Lopreiato, A. Scotto d'Abusco, F. Valentini, E. Placidi, F. Arciprete, A. Martinelli, A. Piozzi, Graphene oxide oxygen content affects physical and biological properties of scaffolds based on chitosan/graphene oxide conjugates, Materials 12 (7) (2019) 1142.

[54] S. Suvarnapathaki, X. Wu, T. Zhang, M.A. Nguyen, A.A. Goulopoulos, B. Wu, G. Camci-Unal, Oxygen generating scaffolds regenerate critical size bone defects, Bioact. Mater. 13 (2022) 64–81.

[55] S.D. Dutta, K. Ganguly, M.-S. Jeong, D.K. Patel, T.V. Patil, S.-J. Cho, K.-T. Lim, Bioengineered lab-grown meat-like constructs through 3D bioprinting of antioxidative protein hydrolysates, ACS Appl. Mater. Interfaces 14 (30) (2022) 34513–34526.

[56] R. Schmid, S.K. Schmidt, R. Detsch, H. Horder, T. Blunk, S. Schrüfer, D. W. Schubert, L. Fischer, I. Thievessen, S. Heltmann-Meyer, A new printable alginate/hyaluronic acid/gelatin hydrogel suitable for biofabrication of in vitro and in vivo metastatic melanoma models, Adv. Funct. Mater. 32 (2) (2022) 2107993.

[57] H. Sun, J. Xu, Y. Wang, S. Shen, X. Xu, L. Zhang, Q. Jiang, Bone microenvironment regulative hydrogels with ROS scavenging and prolonged oxygen-generating for enhancing bone repair, Bioact. Mater. 24 (2023) 477–496.

[58] A. Motealleh, A.H. Schäfer, O. Fromm, N.S. Kehr, 3D-printed oxygen-carrying nanocomposite hydrogels for enhanced cell viability under hypoxic and normoxic conditions, Biomacromolecules 22 (11) (2021) 4758–4769.

[59] L. Wang, D. Li, Y. Huang, R. Mao, B. Zhang, F. Luo, P. Gu, P. Song, X. Ge, J. Lu, Bionic mineralized 3D-printed scaffolds with enhanced in situ mineralization for cranial bone regeneration, Adv. Funct. Mater. (2023) 2309042.

[60] A.J. Seymour, S. Shin, S.C. Heilshorn, 3D printing of microgel scaffolds with tunable void fraction to promote cell infiltration, Adv. Healthcare Mater. 10 (18) (2021) 2100644.

[61] A. Zhang, L. Sun, K. Chen, C. Liu, Y. Yuan, 3D printing viscoelastic hydrogel-based scaffolds with a swelling-dependent gate for cartilage injury regeneration, Chem. Eng. J. 480 (2024) 147260.

[62] M. Orecchioni, Y. Ghosheh, A.B. Pramod, K. Ley, Macrophage polarization: different gene signatures in M1 (LPS+) vs. classically and M2 (LPS–) vs. alternatively activated macrophages, Front. Immunol. 10 (2019) 1084.

[63] K. Buscher, E. Ehinger, P. Gupta, A.B. Pramod, D. Wolf, G. Tweet, C. Pan, C. D. Mills, A.J. Lusis, K. Ley, Natural variation of macrophage activation as disease-relevant phenotype predictive of inflammation and cancer survival, Nat. Commun. 8 (1) (2017) 16041.

[64] Z. Chen, C. Wu, W. Gu, T. Klein, R. Crawford, Y. Xiao, Osteogenic differentiation of bone marrow MSCs by β-tricalcium phosphate stimulating macrophages via BMP2 signalling pathway, Biomaterials 35 (5) (2014) 1507–1518.

[65] W. Wang, Q. Liu, Y. Zhang, L. Zhao, Involvement of ILK/ERK1/2 and ILK/p38 pathways in mediating the enhanced osteoblast differentiation by micro/nanotopography, Acta Biomater. 10 (8) (2014) 3705–3715.

[66] L. Liu, Y. Miao, X. Shi, H. Gao, Y. Wang, Phosphorylated chitosan hydrogels inducing osteogenic differentiation of osteoblasts via JNK and p38 signaling pathways, ACS Biomater. Sci. Eng. 6 (3) (2020) 1500–1509.

[67] X. Shi, S.H. Sung, J.H. Chau, Y. Li, Z. Liu, R.T. Kwok, J. Liu, P. Xiao, J. Zhang, B. Liu, Killing G (+) or G (−) bacteria? The important role of molecular charge in AIE-active photosensitizers, Small Methods 4 (7) (2020) 2000046.

[68] D. He, H. Yang, D. Jin, J. Qu, X. Yuan, Y.-n. Zhang, M. Huo, W.J. Peijnenburg, Rapid water purification using modified graphitic carbon nitride and visible light, Appl. Catal. B Environ. 285 (2021) 119864.

[69] A.H. Asif, N. Rafique, R.A.K. Hirani, L. Shi, S. Zhang, S. Wang, H. Sun, Graphitic carbon nitride engineered α-Fe2O3/rGO heterostructure for visible-light-driven photochemical oxidation of sulfamethoxazole, Chem. Eng. J. 451 (2023) 138630.

[70] Y. Guo, Y. Wang, X. Zhao, X. Li, Q. Wang, W. Zhong, K. Mequanint, R. Zhan, M. Xing, G. Luo, Snake extract–laden hemostatic bioadhesive gel cross-linked by visible light, Sci. Adv. 7 (29) (2021) eabf9635.

[71] H. Yuk, J. Wu, T.L. Sarrafian, X. Mao, C.E. Varela, E.T. Roche, L.G. Griffiths, C. S. Nabzdyk, X. Zhao, Rapid and coagulation-independent haemostatic sealing by a paste inspired by barnacle glue, Nat. Biomed. Eng. 5 (10) (2021) 1131–1142.

[72] S.S. Biranje, J. Sun, L. Cheng, Y. Cheng, Y. Shi, S. Yu, H. Jiao, M. Zhang, X. Lu, W. Han, Development of cellulose nanofibril/casein-based 3D composite hemostasis scaffold for potential wound-healing application, ACS Appl. Mater. Interfaces 14 (3) (2022) 3792–3808.

[73] A. Mahmoodzadeh, J. Moghaddas, S. Jarolmasjed, A.E. Kalan, M. Edalati, R. Salehi, Biodegradable cellulose-based superabsorbent as potent hemostatic agent, Chem. Eng. J. 418 (2021) 129252.

[74] S. Singh, J. Dodt, P. Volkers, E. Hethershaw, H. Philippou, V. Ivaskevicius, D. Imhof, J. Oldenburg, A. Biswas, Structure functional insights into calcium binding during the activation of coagulation factor XIII A, Sci. Rep. 9 (1) (2019) 11324.

[75] G. Xi, W. Liu, M. Chen, Q. Li, X. Hao, M. Wang, X. Yang, Y. Feng, H. He, C. Shi, Polysaccharide-based lotus seedpod surface-like porous microsphere with precise and controllable micromorphology for ultrarapid hemostasis, ACS Appl. Mater. Interfaces 11 (50) (2019) 46558–46571.

[76] D. Zhang, F. Peng, J. Tan, Y. Zhang, F. Wang, J. Xie, R. Xu, H. Du, S. Qian, Y. Qiao, Self-assembled ferric oxyhydroxide nanosheet on PEO-coated magnesium alloy with photocatalytic/photothermal antibacterial and enhanced osteogenesis activities, Chem. Eng. J. 437 (2022) 135257.

[77] C. Xiao, R. Wang, R. Fu, P. Yu, J. Guo, G. Li, Z. Wang, H. Wang, J. Nie, W. Liu, Piezo-enhanced near infrared photocatalytic nanoheterojunction integrated injectable biopolymer hydrogel for anti-osteosarcoma and osteogenesis combination therapy, Bioact. Mater. 34 (2024) 381–400.

[78] M. Wu, Y. Zhang, P. Wu, F. Chen, Z. Yang, S. Zhang, L. Xiao, L. Cai, C. Zhang, Y. Chen, Mussel-inspired multifunctional surface through promoting osteogenesis and inhibiting osteoclastogenesis to facilitate bone regeneration, NPJ Regenerative medicine 7 (1) (2022) 29.

[79] T. Wang, J. Bai, M. Lu, C. Huang, D. Geng, G. Chen, L. Wang, J. Qi, W. Cui, L. Deng, Engineering immunomodulatory and osteoinductive implant surfaces via mussel adhesion-mediated ion coordination and molecular clicking, Nat. Commun. 13 (1) (2022) 1–17.

[80] J. Zhang, D. Tong, H. Song, R. Ruan, Y. Sun, Y. Lin, J. Wang, L. Hou, J. Dai, J. Ding, Osteoimmunity-regulating biomimetically hierarchical scaffold for augmented bone regeneration, Adv. Mater. 34 (36) (2022) 2202044.

[81] J. Zhou, M. Li, Y. Hui, C. Li, J. Chang, B. Chen, C. Wang, W. Guo, T. Wang, Hemostatic sponge based on easily prepared crosslinked gelatin and sodium alginate for wound healing, J. Mater. Sci. (2024) 1–19.

[82] V.P. Reis, M.V. Paloschi, C.M.A. Rego, M.N.M. Tavares, C.N. Boeno, J.A. Lopes, A. F. Ferreira, A.M. Soares, S.R. Zamuner, J.P. Zuliani, Photobiomodulation induces murine macrophage polarization toward M2 phenotype, Toxicon (2021) 171–175.

[83] H. Kang, K. Zhang, D.S.H. Wong, F. Han, B. Li, L. Bian, Near-infrared light-controlled regulation of intracellular calcium to modulate macrophage polarization, Biomaterials (2018) 681–696.